OPEN ACCESS



The COS-Holes Survey: Connecting Galaxy Black Hole Mass with the State of the CGM

Samantha L. Garza¹, Jessica K. Werk¹, Benjamin D. Oppenheimer², Kirill Tchernyshyov¹, N. Nicole Sanchez^{3,4}, Yakov Faerman 1, Kate H. R. Rubin 5,6, Misty C. Bentz 0, Jonathan J. Davies 0, Joseph N. Burchett 0, Robert A. Crain 10, and J. Xavier Prochaska 11,12,13 ¹ Department of Astronomy, University of Washington, Seattle, WA 98195, USA; samgarza@uw.edu Center for Astrophysics and Space Astronomy, 389 UCB, Boulder, CO 80309, USA ³ Carnegie Observatories, 813 Santa Barbara Street, Pasadena, CA 91101 USA ⁴ California Institute of Technology, TAPIR 350-17, 1200 E. California Boulevard, Pasadena, CA 91125-0001 USA Department of Astronomy, San Diego State University, San Diego, CA 92182 USA ⁶ Department of Astronomy & Astrophysics, University of California, San Diego, La Jolla, CA 92093, USA Department of Physics and Astronomy, Georgia State University, Atlanta, GA 30303, USA ⁸ Department of Physics and Astronomy, University College London, Gower Street, London, WC1E 6BT, UK Department of Astronomy, New Mexico State University, Las Cruces, NW 88003, USA Astrophysics Research Institute, Liverpool John Moores University, 146 Brownlow Hill, Liverpool, L3 5RF, UK Department of Astronomy and Astrophysics, University of California, Santa Cruz, CA 95064, USA ¹² Kavli Institute for the Physics and Mathematics of the Universe (Kavli IPMU), 5-1-5 Kashiwanoha, Kashiwa, 277-8583, Japan ¹³ Division of Science, National Astronomical Observatory of Japan, 2-21-1 Osawa, Mitaka, Tokyo, 181-8588, Japan Received 2024 January 19; revised 2024 April 25; accepted 2024 May 20; published 2024 July 24

Abstract

We present an analysis of Hubble Space Telescope COS/G160M observations of C IV in the inner circumgalactic medium (CGM) of a novel sample of eight $z\sim0$, $L\approx L^*$ galaxies, paired with UV-bright QSOs at impact parameters ($R_{\rm proj}$) between 25 and 130 kpc. The galaxies in this stellar-mass-controlled sample ($\log_{10}M_{\star}/M_{\odot}\sim10.2-10.9~M_{\odot}$) host supermassive black holes (SMBHs) with dynamically measured masses spanning $\log_{10}M_{\rm BH}/M_{\odot}\sim6.8-8.4$; this allows us to compare our results with models of galaxy formation where the integrated feedback history from the SMBH alters the CGM over long timescales. We find that the C IV column density measurements ($N_{\rm C\,IV}$; average $\log_{10}N_{\rm C\,IV,CH}=13.94\pm0.09~{\rm cm}^{-2}$) are largely consistent with existing measurements from other surveys of $N_{\rm C\,IV}$ in the CGM (average $\log_{10}N_{\rm C\,IV,Lit}=13.90\pm0.08~{\rm cm}^{-2}$), but do not show obvious variation as a function of the SMBH mass. By contrast, specific star formation rate (sSFR) is highly correlated with the ionized content of the CGM. We find a large spread in sSFR for galaxies with $\log_{10}M_{\rm BH}/M_{\odot}>7.0$, where the CGM C IV content shows a clear dependence on galaxy sSFR but not $M_{\rm BH}$. Our results do not indicate an obvious causal link between CGM C IV and the mass of the galaxy's SMBH; however, through comparisons to the EAGLE, Romulus25, and IllustrisTNG simulations, we find that our sample is likely too small to constrain such causality.

Unified Astronomy Thesaurus concepts: Galaxy formation (595); Circumgalactic medium (1879); Quasar absorption line spectroscopy (1317)

1. Introduction

For decades, absorption-line experiments using bright background quasars (QSOs) have been recognized as an efficient way of studying diffuse gaseous atmospheres of the Milky Way and other galaxies (e.g., Bahcall & Spitzer 1969; Bergeron 1986; Werk et al. 2013). With the more recent addition of results from Hubble Space Telescope (HST) / COS, astronomers have established that this diffuse outer part of galaxies, called the circumgalactic medium (CGM), is a highly ionized, massive, spatially extended reservoir of both fuel for future star formation and the byproducts of stellar evolution (Lehner & Howk 2011; Peeples et al. 2014; Werk et al. 2014; Tumlinson et al. 2017). The properties of the CGM, particularly the highly ionized CGM traced by O VI, are linked to the star-forming properties of host galaxies (e.g., Tumlinson et al. 2011; Tchernyshyov et al. 2022). For this reason, the CGM can serve as an excellent testing ground for astrophysical models of galaxy-scale feedback. In this work, we focus on

Original content from this work may be used under the terms of the Creative Commons Attribution 4.0 licence. Any further distribution of this work must maintain attribution to the author(s) and the title of the work, journal citation and DOI.

testing the cumulative effect of feedback from supermassive black holes (SMBHs) on the content of the cool CGM.

It is well known that the properties of galactic SMBHs correlate with their parent galaxy properties. For example, Kormendy & Richstone (1995) found that black hole masses scale linearly with the absolute luminosity of the host bulge (or elliptical galaxy). This result inspired many investigations into other scaling relationships between these galaxy properties and their corresponding central black hole properties, which found an indirect link between galaxy formation and the growth of their SMBHs (Haehnelt et al. 1998; Magorrian et al. 1998; Saglia et al. 2016). In particular, both the relation between the mass of the central SMBH and the stellar dispersion of its host galaxy's bulge, $M_{\rm BH}$ - σ , and the bulge mass- $M_{\rm BH}$ correlation (Silk & Rees 1998; Ferrarese & Merritt 2000; Gebhardt et al. 2000; Häring & Rix 2004; Reines & Volonteri 2015) reflect the assertion that the mass of the SMBH is a fundamental property of a galaxy, reflective of its history (Kormendy & Ho 2013; van den Bosch 2016). To extend this further, we posit that there can be a significant (and observable) alteration of the CGM content of galaxies due to black hole activity over time due to the cumulative effect of the processes associated with black hole

growth such as those envisioned in most kinetic-mode feedback scenarios (e.g., Best & Heckman 2012).

Recently, analytical studies have shown that maintaining the large observed column densities of highly ionized gas in the CGM, traced by far-ultraviolet (FUV) transitions like O VI, for longer than a gigayear requires a significant source of energy that cannot be supplied by galactic supernovae and stellar winds alone (Mathews & Prochaska 2017, but see Faerman et al. 2020, 2022). If these are the only energy sources, McQuinn & Werk (2018) assert that much of a galaxy's energy budget must be expended in the CGM (rather than the interstellar medium). SMBHs may provide a promising source of far-reaching intermittent feedback shocks that can keep the gas in the CGM warm and highly ionized $(T > 10^3)$. More specifically, the energy released from building an SMBH not only exceeds the binding energy of the gas in the bulge (by orders of magnitude), but can easily exceed the binding energy of the entire gaseous halo (Oppenheimer 2018). Therefore, even with a low efficiency of the SMBH rest-mass energy being imparted to the gaseous halo over its history, the mass and the energetics of the CGM can be significantly affected.

In combination with established black hole scaling relations, these arguments imply that the mass of an SMBH may be a key determinant for the content and kinematics of the CGM around L^* galaxies. There are already established physical links (i.e., scaling relationships) for galaxies on black hole scales (subparsec) and stellar-disk scales (kiloparsec). If these relationships are combined with the expectation that the extended gaseous halos of galaxies fuel their star formation, it is possible that the evolution of a galaxy's central black hole likewise physically links to the properties of galactic gas on CGM scales (tens to hundreds of kiloparsecs). Our present survey, which we call COS-Holes, seeks to examine whether such a correlation exists between the parsec-scale physics of black hole growth and the global, kiloparsec-scale gas flows of the CGM that fuel star formation (Nelson et al. 2018a; Sanchez et al. 2019; Oppenheimer et al. 2020).

In the last five years, simulation work has already suggested that feedback from a galaxy's SMBH impacts the content and ionization state of its CGM, but studies have differing views on the role the SMBH ultimately plays. Results from studies using the cosmological simulations TNG (Nelson et al. 2018b), EAGLE (Davies et al. 2019; Oppenheimer et al. 2020), and ROMULUS (Tremmel et al. 2017) suggest that the SMBH at the center of galaxies enriches the CGM by driving metals out of the disk and into the halo. However, in EAGLE and TNG, galaxies that host more massive black holes (BHs) can provide a significant amount of energy over time that transports baryons beyond the virial radius, ultimately reducing gas accretion, overall star formation, and the total density of the CGM. Using O VI, demonstrated to be a sensitive probe of SMBH feedback, Sanchez et al. (2019) reports a contrasting view to the role of the SMBH outlined above. Results from ROMULUS do not show evacuation of CGM gas into the intergalactic medium, but rather suggest that galaxies with more massive BHs are more likely to have a more metal-enriched (higher ion column density) CGM. Due to these opposing simulation predictions, it is imperative to empirically test the role SMBH feedback plays (if any) in setting the content of the CGM.

This work examines the observed relationship, if any, between black hole growth over long timescales (parameterized by a dynamically measured SMBH mass) and the gas content

and kinematics within the extended halos of galaxies. In addition, we compare these observations to predictions from cosmological simulations. Our novel sample of stellar- and halo-mass controlled nearby galaxies (z < 0.005; Figure 1) hosts a wide range of dynamically resolved SMBHs ($\log_{10} M_{\rm BH} \sim 6.8-8.4$) and FUV-bright QSOs at impact parameters of $25 < R_{\rm proj} < 130\,{\rm kpc}$.

This paper proceeds as follows: Section 2 describes the sample selection (Section 2.1), FUV spectroscopy (Section 2.1.1), and data reduction and analysis for the COS-Holes sample (Section 2.3); Section 3 presents the BH mass estimates for archival data collected to increase the sample size; Section 4 presents general trends for the COS-Holes sample (Section 4.1), the radial profile for the COS-Holes+Literature sample (Section 4.2), multivariate analysis and statistics done on the sample (Section 4.2.1), and the minimum mass of carbon seen in the CGM of the sample (Section 4.3); Section 5 describes the three simulations used in this paper (Section 5.1) and presents the results of the simulated values compared to the results of the combined sample (Section 5.3); Section 6 presents a discussion of sSFR dependence in C_{IV} ionization (Section 6.1) and whether BHs evacuate their CGMs or not (Section 6.2); lastly we present a summary of our conclusions in Section 7. In this work, we assume a flat-Universe ΛCDM cosmology with $H_0 = 67.8 \,\mathrm{km \, s^{-1} \, Mpc^{-1}}$ and $\Omega_m = 0.308$ (Planck Collaboration et al. 2016).

2. Observation and Data Analysis

2.1. Sample Selection

The COS-Holes Survey consists of nine UV-bright QSOs, z < 0.005, probing the halos of eight galaxies at impact parameters $R_{\rm proj} \sim 25-130 \, \rm kpc$ as seen in Figure 1. To build the survey, we cross matched the Sloan Digital Sky Survey (SDSS) DR14 QSO catalog (Pâris et al. 2018) and the UVQS (Monroe et al. 2016) QSO catalogs with several published catalogs of galaxy BH masses (Kormendy & Ho 2013; McConnell & Ma 2013; Bentz & Katz 2015; Läsker et al. 2016; van den Bosch 2016; Terrazas et al. 2017) to search for FUV-bright QSOs (Galaxy Evolution Explorer (GALEX) $M_{FUV} < 19$) within 150 kpc projected distance from the galaxies in their rest frames. By design, the resulting sample contains galaxies that have dynamically determined SMBH masses (e.g., through stellar dynamics, ionized gas dynamics, CO molecular gas disk dynamics, maser disk dynamics, etc.). We note that we did not select our galaxies based on assembly history or morphology. We acknowledge that recent results have shown that disruptions in the disk (either by merger or similar event) can be an important factor for how BHs grow and affect the CGM (Davies et al. 2022, 2024); however testing for these morphological differences in the galaxies and how that affects the properties of the CGM is beyond the scope of this work. The property cuts implemented for our sample, as described below, were strategically made to match similar cuts made for previous surveys searching for highly ionized gas (COS-Halos; Tumlinson et al. 2011; Werk et al. 2012) within the cool and intermediate temperature phase of the CGM (Tumlinson et al. 2017); what sets our sample apart, however, is our focus on galaxies that have accurately measured BH masses in order to determine how they impact the state of the CGM.

To start, we eliminate from the sample any galaxies in dense cluster environments (e.g., Virgo) that have already been shown

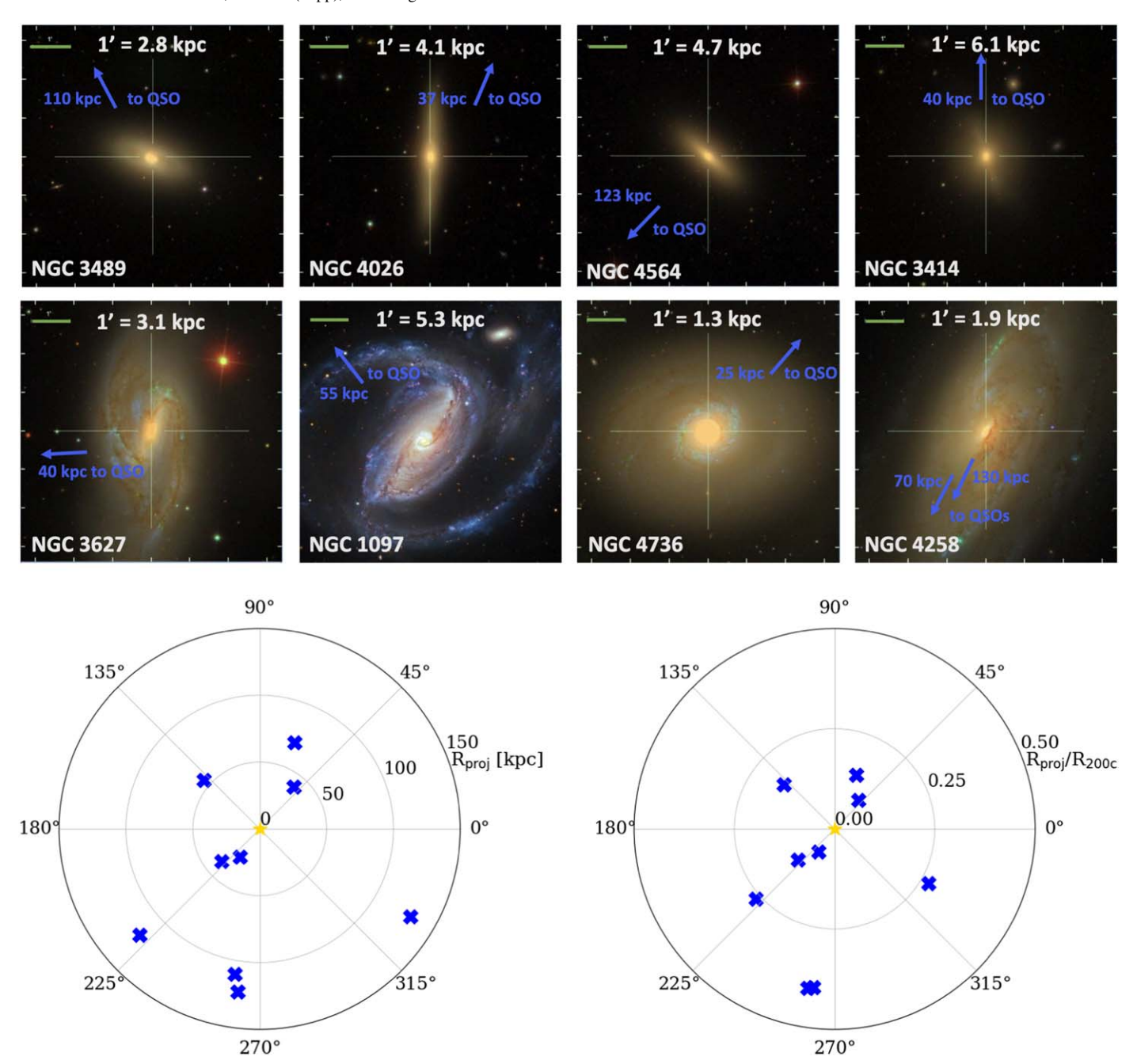


Figure 1. Top: Sloan Digital Sky Survey images of each of the eight target galaxies in the sample, with exception of NGC 1097 with the image from ESO. The physical scale (in kpc) in each galaxy's rest frame is shown at the top of its $6^{\circ} \times 6^{\circ}$ stamp. The targeted QSOs lie outside of the shown field of view; blue arrows and text display the direction and distance to each FUV-bright QSO. One galaxy, NGC 4258, has two UV-bright QSOs at <130 kpc. Bottom: target figure showing the distribution of QSO position angles (blue x's) on the sky with respect to the target galaxies (shifted to the center, yellow star). On the left, the radial coordinate (R_{proj}) is in physical kpc at the galaxy redshift, and on the right, this coordinate is translated to the fraction of galaxy virial radius, R_{proj}/R_{200c} , at which the sight line intercepts the halo. No knowledge of galaxy disk orientation or inclination with respect to the sight line is implied here.

to possess significantly less gas than galaxies in more isolated environments (Yoon et al. 2012; Burchett et al. 2018). We check the GALEX NUV magnitudes of our targets for large values of NUV – FUV colors, which would potentially indicate the presence of a strong Lyman Limit system ($N_{\rm HI} \geqslant 10^{17} \, {\rm cm}^{-2}$; LLS) along the line of sight that may have contaminated our transitions of interest. We note that this process does not introduce a bias to the sample selection since the LLS absorption would be at unrelated higher redshifts than our targets.

It is known that active galactic nucleus (AGN) feedback can be highly directional and not necessarily aligned with the spin axis of the galaxy (Bentz et al. 2023). However, we choose not to include QSOs that probe the halos of galaxies with black holes that are currently accreting as Seyferts or quasars themselves, as done in Berg et al. (2018). Instead, we are more interested in the long-term effects the black hole has on the halo and and thus selected galaxies based on their stellar mass, redshift, and having a dynamically measured black hole mass available. None of the galaxies in our sample is classified as an AGN in the mid-infrared photometrically selected sample of Asmus et al. (2020), using a method that has a 90% reliability in selecting AGN (Assef et al. 2018). We note,

Table 1Galaxy Sample Properties

| Galaxy (1) | R.A. (deg) (2) | Decl. (deg) (3) | z (4) | Morph (5) | D (Mpc) (6) | sSFR (log ₁₀ yr ⁻¹) (7) | M_* $(\log_{10}M_{\odot})$ (8) | $M_{200c} \ (\log_{10} M_{\odot}) \ (9)$ | $M_{ m BH} \ (\log_{10} M_{\odot}) \ (10)$ |
|------------|----------------------|-----------------|----------|-----------|----------------------------|--|----------------------------------|--|--|
| NGC 1097 | 41.579 | -30.275 | 0.0042 | SB(s)b | 14.50 a | -9.7 | 10.5 | 11.75 | 8.14 ± 0.090 |
| NGC 3414 | 162.818 | 27.975 | 0.0049 | S0 | $25.20 \pm 2.74 \text{ b}$ | -11.8 | 10.8 | 12.29 | 8.40 ± 0.07 |
| NGC 3489 | 165.078 | 13.901 | 0.0022 | SABa | 11.98 c | -11.2 | 10.2 | 11.45 | 6.77 ± 0.065 |
| NGC 3627 | 170.063 | 12.991 | 0.0024 | SAB(s)b | $10.05 \pm 1.09 \text{ b}$ | -10.3 | 10.8 | 12.41 | 6.92 ± 0.048 |
| NGC 4026 | 179.855 | 50.962 | 0.0033 | SO | 13.35 с | -12.2 | 10.4 | 11.66 | 8.26 ± 0.120 |
| NGC 4258 | 184.740 | 47.304 | 0.0015 | SABbc | $7.27 \pm 0.50 \text{ b}$ | -10.9 | 10.9 | 12.51 | 7.58 ± 0.030 |
| NGC 4564 | 189.113 | 11.439 | 0.0038 | S0 | 15.94 c | -12.4 | 10.4 | 11.63 | 7.94 ± 0.140 |
| NGC 4736 | 192.721 | 41.121 | 0.0010 | Sab | $5.00\pm0.79~b$ | -10.7 | 10.6 | 11.94 | 6.83 ± 0.120 |

Note. Comments on columns: (1) galaxy name; (2–3) R.A. and decl. for the galaxy; (4) galaxy redshift; (5) morphology; (6) assumed distance to galaxy where the letter beside the distance corresponds to one of the following references: (a) van den Bosch (2016), (b) Saglia et al. (2016), (c) Tonry et al. (2001) SBF corrected via Equation A1 in Blakeslee et al. (2010); (7) specific star formation rate; (8) stellar mass; (9) halo mass; (10) SMBH mass. Regarding sSFRs: typical errors on SFRs derived from infrared photometry are 0.2–0.3 dex (Rieke et al. 2009; Terrazas et al. 2017), while stellar masses are accurate to about \sim 50%. On average, for galaxies of these masses, sSFR errors will be on the order of a few—several tenths of a dex.

Table 2Background QSO Properties

| QSO | R.A. (deg) | Decl. (deg) | z | R _{proj} (kpc) | $R_{\mathrm{proj}}/R_{\mathrm{200c}}$ | Mag (FUV) | Mag (NUV) | $N_{ m ORB}$ |
|-------------------------|---------------|----------------|-------|-------------------------|---------------------------------------|--------------|--------------|--------------|
| (1) | (2) | (3) | (4) | (5) | (6) | (7) | (8) | (9) |
| UVQSJ024649.87-300741.5 | 41.707792 | -30.128194 | 0.524 | 55.66 | 0.32 | 18.46 | 17.9 | 4 |
| SDSSJ105115.75+280527.1 | 162.81564 | 28.090865 | 0.423 | 40.50 | 0.15 | 18.2 | 17.75 | 4 |
| SDSSJ110139.76+142953.4 | 165.4157 | 14.498172 | 0.635 | 110.00 | 0.80 | 18.99 | 18.70 | 7 |
| SDSSJ112304.91+125748.0 | 170.77049 | 12.963349 | 0.315 | 120.00 | 0.42 | 18.76 | 18.34 | 6 |
| SDSSJ115901.72+510630.7 | 179.75718 | 51.108554 | 0.524 | 37.38 | 0.23 | 18.72 | 18.36 | 4 |
| SDSSJ122046.61+464347.5 | 185.19421 | 46.729881 | 0.707 | 69.78 | 0.22 | 18.82 | 18.21 | 6 |
| UVQSJ122208.10+461250.1 | 185.53375 | 46.213917 | 0.111 | 130.30 | 0.42 | 18.30 | 18.11 | 4 |
| LBQS-1235+1123 | 189.43571 | 11.116143 | 0.949 | 123.10 | 0.77 | 18.99 | 17.93 | 7 |
| SDSSJ124939.06+412243.5 | 192.41277 | 41.378773 | 0.368 | 25.52 | 0.13 | 18.62 | 18.55 | 6 |

Note. Comments on columns: (1) QSO identification; (2–3) R.A. and decl. for the QSO; (4) QSO redshift; (5) QSO impact parameter; (6) impact parameter normalized by virial radius; (7) FUV magnitude; (8) NUV magnitude; (9) number of orbits.

however, that many of our galaxies do exhibit LINER-like emission in their central regions, possibly indicating a low-luminosity, accretion-powered active nucleus (e.g., Molina et al. 2018). LINER emission is quite common among nearby, L^* spiral galaxies, and it can be related to AGN phenomena, although this relation is uncertain and poorly quantified (Ho et al. 1997).

In addition, there can be an azimuthal dependence of ion absorption in disk-dominated galaxies. For example, it has been shown that there is a strong azimuthal dependence with Mg II (Bordoloi et al. 2011), but for O VI the correlation along the major and minor axes is less clear (Kacprzak et al. 2019). These dependencies have not been demonstrated for C IV and investigating them in the COS-Holes sample is beyond the scope of this work. Moreover, as seen in Figure 1, some of our galaxies are too face on to report accurate azimuthal angles. The remaining galaxies have azimuthal angles consistent with a random distribution, and thus any azimuthal angle dependence of CGM C IV will not play a significant role in driving the trends (or lack thereof) we observe.

Finally, the nearby galaxy NGC 4258, which has a highly accurate BH mass measurement from megamaser kinematics (Miyoshi et al. 1995), is serendipitously intersected by two inner CGM QSO sight lines at 70 and 130 kpc. We include both QSO targets in our final sample because it offers a rare

opportunity to study subtle variations (e.g., column density, kinematics, etc.) within a single halo.

We selected a sample of galaxies with stellar masses spanning a narrow range around M^* ($\approx 10^{10.5} M_{\odot}$), since stellar mass has been found to correlate with ionized CGM content (e.g., Tchernyshyov et al. 2022). We estimate the halo masses of our sample by following the same method as outlined in CGM² by Tchernyshyov et al. (2022). Using the stellar mass-halo relation, as defined in Tab J1 of Behroozi et al. (2019), in combination with the approach laid out in Hu & Kravtsov (2003), we convert the halo masses to match the convention where the average mass density within the halo radius is 200 times the critical density of the Universe. We denote these halo masses and the corresponding virial radii as M_{200c} and R_{200c} . The final range of stellar and halo masses for the sample are $\log_{10}M_{\star}/M_{\odot} \sim 10.2\text{--}10.9$ and $\log_{10}M_{\rm halo}/M_{\odot} \sim$ 11.45-12.51, respectively. We note that a stellar mass of $\approx 10^{10.5} M_{\odot}$ is representative of L^{\star} galaxies, but also can be a transitional stellar mass in terms of sSFR, which is known to correlate with CGM properties in intermediate ionization states (Tchernyshyov et al. 2023). However, by keeping the range of stellar and halo masses relatively small, we minimize the scatter due to these properties and enable a controlled examination of the role SMBHs and SFR play in shaping the

properties of the CGM. The galaxy and QSO properties for the sample can be found in Tables 1 and 2, respectively.

2.1.1. Star Formation Rates

We obtain star formation rates (SFRs) for the COS-Holes sample from Terrazas et al. (2017) in Section 4. For the three galaxies in our survey not included in their sample (NGC 3489, NGC 4026, and NGC 4564), we calculate their corresponding SFRs using the same methodology; we summarize the procedure here, but a detailed description can be found in Bell (2003) and Terrazas et al. (2016). We calculate far-infrared (FIR) SFRs by using Equation (A1) in Bell (2003), which uses 60 and 100 μ m IRAS fluxes to estimate the FIR flux. We then estimate the total infrared (TIR) flux via TIR = 2 × FIR (Bell 2003). Finally, the TIR-derived SFR is calculated using Equation (12) in Kennicutt & Evans (2012):

$$\log_{10} SFR_{TIR}(M_{\odot} yr^{-1}) = \log_{10} L_{TIR} - 43.41$$
 (1)

where $L_{\rm TIR}$ is the TIR luminosity calculated from the TIR flux estimates and distances to the galaxy (for consistency we use the same distances presented in Terrazas et al. 2017; for more detailed information, see Table 1). We note that for NGC 3489 only 65 and 90 μ m fluxes from AKARI were available on the NASA/IPAC Extragalactic Database, and we use those values to calculate its respective SFR. ¹⁴ To present the calculated SFRs as \log_{10} sSFRs (which range between -12.4 and -9.7) in Table 1, we divide them by the stellar mass of the galaxy. Typical stellar mass uncertainties derived from SDSS photometry are $\pm 50\%$ (Kauffmann et al. 2003; Blanton & Roweis 2007; approximately 0.2 dex), and the SFR errors derived from infrared photometry are approximately 0.2–0.3 dex (Rieke et al. 2009; Terrazas et al. 2017).

2.2. COS Spectroscopy

The quasar spectra for the COS-Holes Survey were taken using the G160M grating on the Cosmic Origins Spectrograph (COS; Froning & Green 2009; Green et al. 2012) on the Hubble Space Telescope as a part of a 55 orbit Cycle 29 HST Program (PID# 16650). The primary spectral features of interest were absorption lines from the doublets C IV ($\lambda\lambda$ 1548, 1550) and Si IV ($\lambda\lambda$ 1393, 1402).

C IV is the highest ionization state transition available at these low redshifts (z < 0.005) where dynamical black hole masses are available, and is easily detectable in the UV. We note that C IV is an "intermediate" ion with a potential energy of 47.89 eV required to ionize C III into C IV. In collisional ionization equilibrium (CIE) C IV reaches a peak ion fraction at a temperature of 1.2×10^5 K ($10^{5.1}$) and falls rapidly at higher temperatures, with less than 10% at 1.6×10^5 K ($10^{5.2}$; Gnat & Sternberg 2007). In photoionization equilibrium (PIE), it peaks at a density of $n_H \approx 2 \times 10^{-5}$ cm⁻³ at z = 0 (Haardt & Madau 2012; Khaire & Srianand 2019). Thus, in CGM conditions, it can form either through photoionization or collisional ionization (Tumlinson et al. 2017). In EAGLE, Oppenheimer et al. (2020) found that C IV is a very good tracer of CGM gas between $T = 10^4 - 10^5$ K and $n_H = 10^{-5} - 10^{-3}$ cm⁻³. While it is beyond the scope of this work to constrain the precise phase of

C IV, we highlight that we are explicitly avoiding characterization of the hot CGM ($T \approx 10^6$ K).

The COS-Holes QSOs have FUV magnitudes of 18.2–19.0 and redshifts ranging from 0.3 to 0.9, and we observed each target QSO for between four and seven orbits in G160M with a central wavelength of 1577 Å. Our exposure times were calculated to detect a 40 mÅ feature at 2σ , consistent with detected C IV around \sim 0.1–1 L^{\star} galaxies in the literature (Borthakur et al. 2013; Bordoloi et al. 2014; Burchett et al. 2016). All spectra achieved a signal-to-noise ratio (S/N) of 10–12 per resel at the wavelengths of C IV.

We combine the CALCOS-generated x1D files using v3.1.1 of the COADD X1D routine provided by the COS-GTO team (Danforth et al. 2016), which properly treats the error arrays of the input files using Poisson statistics. The code aligns the different exposures by determining a constant offset determined by cross-correlating strong ISM lines in a 10 Å wide region of the spectrum. The COS line-spread function (LSF) is well described by a Gaussian convolved with a power law that extends to many tens of pixels beyond the line center (Green et al. 2012). These broad wings affect both the precision of our equivalent width measurements and complicate assessments of line saturation. We mediate these effects by fitting absorption lines with Voigt profiles that incorporate the COS LSF. Each COS resolution element at $R \sim 18,000$ covers 16 km s^{-1} and is sampled by six raw pixels. We perform our analysis on the data binned by three native spectral pixels to a dispersion of $\Delta\lambda \approx$ 0.0367 Å. The resulting science-grade spectra are characterized by a FWHM $\approx 16 \, \text{km s}^{-1}$. We perform continuum fitting with the linetools package, an open-source code for analysis of 1D spectra. 15

2.3. Absorption-line Measurements

This section describes the methods used to measure and calculate key observational properties, presented in Table 3. Section 4 discusses the column densities versus key galaxy parameters (Figure 3).

2.3.1. Line Identification with PyIGM

We manually assign line identifications and redshifts to all absorption features in the spectra using the PyIGM IGMGuesses $GUI.^{16}$ To make sure that we correctly attribute absorption to a COS-Holes galaxy's CGM rather than another absorber at a different redshift, we implement the following methodology. First, we identify absorption features at z = 0, the redshift of the Milky Way. We then identify any "proximate" absorption at the redshift of the QSO observed. Finally, we examine the spectra for Lyman series lines at redshifts $\langle z_{OSO} \rangle$ to find serendipitous absorption systems. After identifying these features, we move to the redshift of the target galaxy to look for any absorption features within \sim 300 km s⁻¹ associated with C IV ($\lambda\lambda$ 1548, 1550), similar to the COS-Halos Survey (Werk et al. 2013). For this paper we specifically focus on C IV identifications and analysis even though other ions (e.g., Si IV $\lambda\lambda 1393$, 1402) were observable; in future work we plan on analyzing other ion absorption features present. We obtain preliminary line profile fits including the following parameters: central velocity v, column density N, and Doppler parameter, b;

¹⁴ The NASA/IPAC Extragalactic Database (NED) is funded by the National Aeronautics and Space Administration and operated by the California Institute of Technology.

¹⁵ https://doi.org/10.5281/zenodo.1036773

¹⁶ https://doi.org/10.5281/zenodo.1045480

Table 3
COS-Holes Measurements

| Galaxy | QSO ID | $z_{ m abs}$ | $\frac{\log_{10}N_{\rm C~IV}}{({\rm cm}^{-2})}$ | $b 	ext{(km s}^{-1})$ | EW (mÅ) | $\frac{ v_{\rm rel} }{(\text{km s}^{-1})}$ |
|----------|-----------|--------------|---|-----------------------|--------------------|--|
| (1) | (2) | (3) | (4) | (5) | (final) (6) | (7) |
| NGC 1097 | UVQSJ0246 | 0.00426 | 14.14 ± 0.05 | 55.60 ± 7.58 | 323.84 ± 33.38 | 2.01 |
| NGC 1097 | UVQSJ0246 | 0.00471 | 13.71 ± 0.10 | 15.36 ± 6.09 | 109.54 ± 27.27 | 145.38 |
| NGC 3414 | SDSSJ1051 | 0.00443 | 13.88 ± 0.05 | 35.26 ± 6.06 | 235.30 ± 26.86 | 148.32 |
| NGC 3489 | SDSSJ1101 | 0.00229 | 13.44 ± 0.10 | 22.95 ± 8.90 | 106.52 ± 19.55 | 30.88 |
| NGC 3627 | SDSSJ1123 | 0.00287 | 13.89 ± 0.07 | 85.00 ± 18.33 | 230.70 ± 41.64 | 152.24 |
| NGC 4026 | SDSSJ1159 | 0.0033 | <13.24 | | <73.10 | 0 |
| NGC 4258 | SDSSJ1220 | 0.001494 | <13.47 | ••• | < 60.32 | 0 |
| NGC 4258 | UVQSJ1222 | 0.001494 | <13.39 | | < 50.20 | 0 |
| NGC 4564 | LBQS-1235 | 0.0038 | <13.40 | | < 58.21 | 0 |
| NGC 4736 | SDSSJ1249 | 0.00054 | 13.75 ± 0.05 | 32.39 ± 6.30 | 186.38 ± 17.07 | 148.55 |
| NGC 4736 | SDSSJ1249 | 0.00083 | 13.48 ± 0.10 | 11.53 ± 6.33 | 95.97 ± 12.53 | 47.32 |
| NGC 4736 | SDSSJ1249 | 0.00111 | 13.86 ± 0.05 | 37.78 ± 5.91 | 217.64 ± 19.25 | 43.94 |

Note. Comments on columns: (1) galaxy name; (2) QSO identification that is shortened from full name; (3) redshift of the absorption coefficient; (4) C IV column density; (5) Doppler parameter; (6) equivalent width; (7) absolute value relative velocity of absorption component projected along the line of sight in the galaxy's frame.

we then input these user specified parameters into a Voigt profile fitting program.

2.3.2. Voigt Profile Fitting

Based on the identifications from the PyIGM IGMGuesses GUI, we measure C IV column densities, Doppler parameter, and the relative velocity of the absorption components using Voigt profile fitting with the package veeper, which uses scipy. optimize.least squares (Virtanen et al. 2020) to perform a least-squares minimization. 17 In five of our OSOgalaxy line-of-sight pairs we detect C IV, while the other four were nondetections and we report them as upper limits. In the spectral regions with no detected metal absorption, we calculate a 2σ upper limit on the column density as estimated by the apparent optical depth method (AODM) with the linetools XSpectrum1D package 18 over a 100 km s⁻¹ velocity span centered on the galaxy redshift. By default, we use the stronger line at 1548 Å to estimate 2σ equivalent width upper limits, similar to the AODM, using linetools XSpectrum1D, but in cases where there is blending or contamination we use the 1550 A line. When multiple absorption components are found in a galaxy's search window, their column densities are summed, and then this total column density is associated with the galaxy. Figure 2 displays the line profile for the C_{IV} ($\lambda\lambda$ 1548, 1550) absorption doublet for NGC 3414 as a representative Voigt profile for the entire COS-Holes sample. The spectra showing C IV (or upper limits) for the rest of the survey are presented in Appendix A.

3. Archival Observations and BH Mass Estimations

We increase our sample size with CGM C IV measurements using published HST/COS data from Borthakur et al. (2013; starbursts), Werk et al. (2013; COS-Halos), Bordoloi et al. (2014; COS-Dwarfs), and Lehner et al. (2020; Project AMIGA). M31 has a measured SMBH mass of $\log_{10}M_{\rm BH}/M_{\odot}=8.15\pm0.24$ (Davis et al. 2017) and a stellar mass of $\log_{10}M_{\star}/M_{\odot}=10.9\pm0.22$ (Williams et al. 2017), both of which are within range of the COS-Holes galaxy properties.

Through the use of several QSO sight lines, it has a wellstudied CGM (Project AMIGA; Lehner et al. 2020). To match the COS-Holes sample we only include sight lines from Project AMIGA if their corresponding impact parameter was ≤150 kpc and did not have any contamination from the Magellanic Stream; for a more detailed explanation of how this contamination was removed, see Lehner et al. (2020). If a sight line contained C IV and had multiple absorption features, we sum the measured N_{CIV} to present a total column density, similar to COS-Halos. We note that having a plethora of QSO sight lines provides the opportunity to compare single QSOgalaxy sight line derived CGM properties to a galaxy with multiple sight lines. However, with this reduced sample of Project AMIGA observations, we choose to take an average of the column densities to represent a singular mean $N_{\rm C\,IV}$ for the Project AMIGA observations. This allows us to have a consistent literature sample and not bias any results toward features seen in M31.

Similar to M31, we only include $N_{\rm C\ IV}$ measurements from galaxies if they had a stellar mass that fell within the range of our COS-Holes observations ($\log_{10}M_{\star}/M_{\odot}=10^{10}-10^{11}$); by making these cuts we add four galaxies from Borthakur et al. (2013), five from Bordoloi et al. (2014), and two from Werk et al. (2013; COS-Halos) to the literature sample. Since galaxies from these surveys do not have dynamically measured BH masses, we estimate the SMBH mass for each galaxy using the following approximation from Equation (7) in Saglia et al. (2016) and Piotrowska et al. (2022):

$$\log_{10} M_{\rm BH} = 5.246 \times \log_{10} \sigma_c - 3.77 \tag{2}$$

where σ_c is the central stellar velocity dispersion of the galaxy, or the random line-of-sight motion of stars due to the galaxy's gravitational potential well.

We obtain central stellar velocity dispersion measurements from the SDSS DR7 value-added catalog ¹⁹ (Abdurro'uf et al. 2022) for our selected sample of galaxies from Borthakur et al. (2013) and Bordoloi et al. (2014). These SDSS σ_c values are the superposition of many individual stellar spectra that were Doppler shifted due to the star's motion within each galaxy and their measurements were made by analyzing the integrated

¹⁷ https://doi.org/10.5281/zenodo.10993983

¹⁸ https://doi.org/10.5281/zenodo.1036773

¹⁹ gal_info_dr7_v5_2.

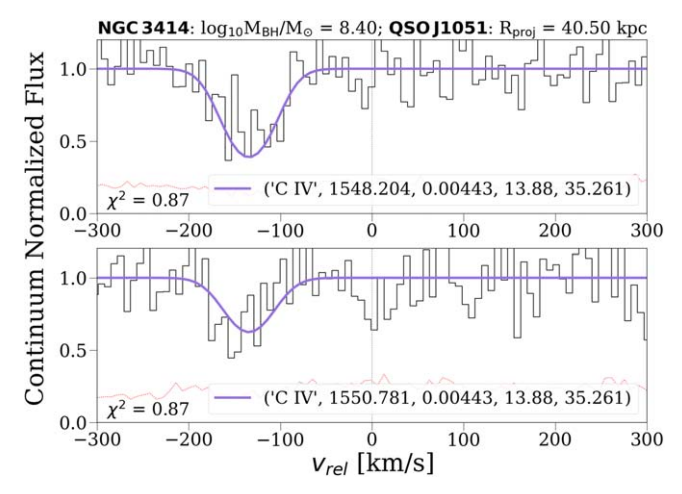


Figure 2. Representative C IV absorption feature of a QSO-galaxy pair (SDSSJ1051–NGC 3414) set in the rest frame of the galaxy. The colored line represents the Voigt profile fit due to the $\lambda\lambda$ 1548, 1550 lines in the top and bottom panels, respectively. The values in the labels correspond to the following: ionic species, wavelength, absorption feature redshift, column density $(\log_{10}N_{\rm C~IV},$ in cm⁻²), and Doppler parameter (km s⁻¹). In the bottom-left-hand corner of the figure is the reduced chi squared for the fit made to each absorption feature. The spectra for the rest of the COS-Holes sample are presented in Appendix A.

spectrum of the whole galaxy. We acknowledge that estimating measurements for σ_c can be complex due to several components that can dominate the integrated spectra, from different stellar populations and/or kinematics in the bulge and the disk. However, these complexities were taken into account in the SDSS catalog where velocity dispersion estimates were only measured for spheroidal systems whose spectra satisfied certain specifications (e.g., galaxy type, z < 0.4, etc.). In addition, it is recommended to only use SDSS velocity dispersion measurements $> 70 \, \mathrm{km \, s^{-1}}$ (due to the SDSS instrumental resolution) for spectra with a median per-pixel $\mathrm{S/N} > 10$; for more information about how these velocity dispersions were measured and how their biases were corrected see Bernardi (2007).

All the galaxies from Borthakur et al. (2013) and Bordoloi et al. (2014); (nine total) have median per-pixel S/N > 10, and the average σ_c value for the galaxies with velocity dispersion measurements $> 70 \text{ km s}^{-1}$ is $111.59 \pm 17.18 \text{ km s}^{-1}$. Four galaxies from Bordoloi et al. (2014) have stellar velocity dispersion measurements $< 70 \,\mathrm{km \, s^{-1}}$. We report these as upper limits and use $70 \,\mathrm{km \, s}^{-1}$ in our $\log_{10} M_{\rm BH} / M_{\odot}$ estimates, which correspond to a value of <5.91. As this is close to the lower bound of the BH mass range for the COS-Holes Survey, and the SDSS fiber spectra are not sensitive to BH estimates lower than this value, we do not believe that adding these BH mass estimations bias the new combined sample. For those galaxies drawn from the COS-Halos sample (Werk et al. 2013), where SDSS fiber spectra of the galaxies were not available, we use the Python package pPXF to analyze the Keck LRIS spectra (COS-Halos; Werk et al. 2012).²⁰ This package calculates a central velocity dispersion from the optical LRIS spectrum; for more clarification on techniques, see Koss et al. (2022). The uncertainties on the BH masses for the literature sample are roughly a factor of 5 larger than those from the COS-Holes sample with dynamically measured BH masses.

We use the package KaplanMeierFitter from the Python package LIFELINES²¹, which implements Greenwood's uncertainty estimate, to determine the average $\log_{10}M_{\rm BH}/M_{\odot}$ for both the literature and the COS-Holes sample. Kaplan-Meier is a nonparametric technique of estimating the survival probability of a set of data and is useful since it assumes that censored observations (upper limits) have the same survival prospects as observations that

limits) have the same survival prospects as observations that continue to be followed. For the literature sample, with 95% confidence intervals, we find the average $\log_{10}M_{\rm BH}/M_{\odot}$ to be 7.40 (6.10, 7.71); this is comparable to the COS-Holes average $\log_{10}M_{\rm BH}/M_{\odot}$ of 7.58 (6.77, 8.255). This sample of 12 additional galaxies adds a wider range of galaxies black hole masses to the sample and statistical power to our analysis, especially in Section 4.2. The collective information for the additional literature sample can be seen in Appendix B in

4. Observational Results

Tables 6 and 7, respectively.

In this section we examine the effects of SMBH feedback on the state of the CGM in $\sim L^*$ galaxies by examining the observational data. The section proceeds as follows: we investigate the relationship, if any, between $N_{\rm C\ IV}$ and $M_{\rm BH}$ for the COS-Holes sample in Section 4.1; Section 4.2 describes analysis for the COS-Holes Survey with the addition of a subset of published literature observations; and Section 4.3 shows our estimate of the minimum mass of carbon in the CGM of our sample.

4.1. COS-Holes General Trends

In Figure 3, we show our measured $N_{\rm C\,IV}$ for each line of sight versus $M_{\rm BH}$; each point is colored by its specific star formation rate (sSFR) and the size scales by impact parameter. We note that the two sight lines that intersect the halo of NGC 4258, colored in gray, are upper limits; even though the upper-limit observations are consistent with each other, studying the variations within this single halo is not possible with these two sight lines. For galaxies with $\log_{10}M_{\rm BH} < 7.0$ we find a 100% covering fraction and a 33% covering fraction for galaxies with $\log_{10}M_{\rm BH} > 7.0$. However, as black hole mass increases we show a large scatter of >1 dex in C IV column density for this range of $M_{\rm BH}$. Due to this wide scatter and how small the sample size is, we suggest that there is no strong identifiable relationship between these two particular properties seen in the COS-Holes observations.

Interestingly, there is a different correlation with another galaxy property; across the $M_{\rm BH}$ range of our sample, galaxies that have low observed C IV column density ($\log_{10}N_{\rm CIV}\lesssim 13.5~{\rm cm}^{-2}$) are less star-forming ($\log_{10}{\rm sSFR}/M_{\star}<-11$) than galaxies with higher observed column density. It is difficult to determine if this trend is due to sample selection and if it is causally or significantly correlated, since several factors could be influencing the C IV content of the CGM. Even so, it raises the question, how much is the SMBH feedback really impacting observed $N_{\rm C\,IV}$ in the CGM, and do other galaxy parameters, like sSFR, play a larger role in setting the ionization state?

²⁰ https://pypi.org/project/ppxf/

²¹ https://doi.org/10.5281/zenodo.10456828

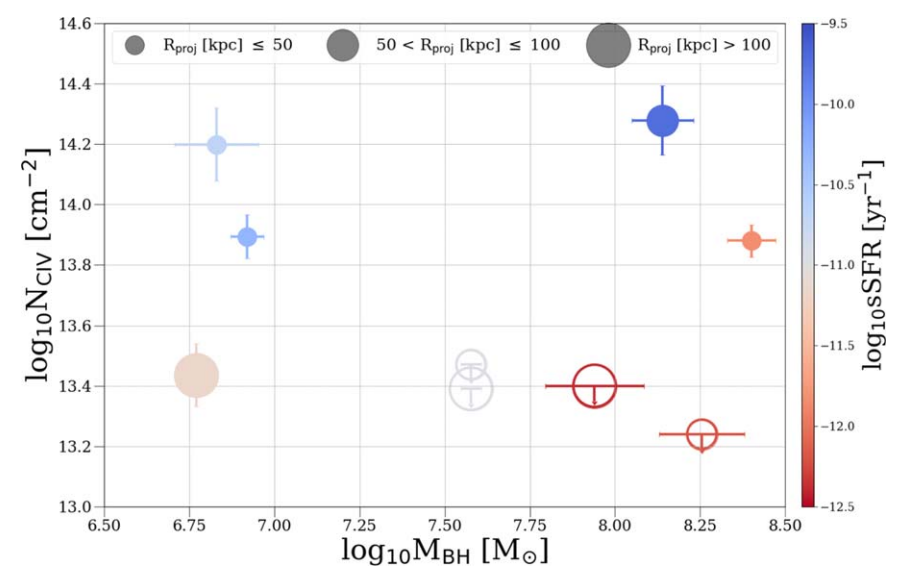


Figure 3. Measured C IV column densities vs. $\log_{10}M_{\rm BH}$. Each data point is colored by the specific star formation rate (sSFR) and each marker size corresponds to the respective impact parameter. Unfilled circles represent 2σ upper limits. There is a wide spread in the C IV column densities as black hole mass increases; interestingly, there is a slight trend with sSFR and column density. Galaxies with low observed column density ($\log_{10}N_{\rm C~IV} \leqslant 13.5$) tend to be less star-forming (sSFR $\lesssim -11.0$) than galaxies with higher observed column density.

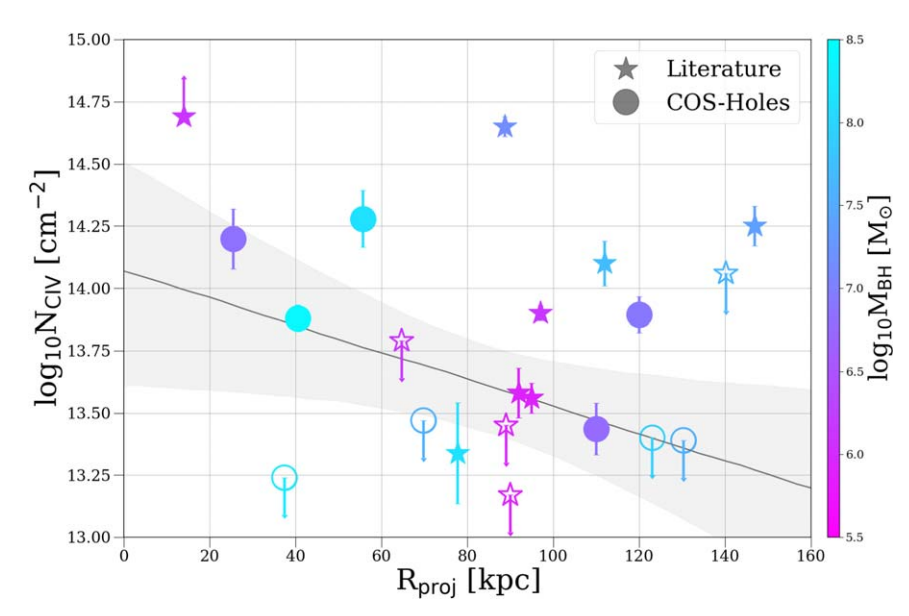


Figure 4. C IV column densities assembled from previous QSO absorption-line surveys probing the CGM of low-z, $\log_{10}M_{\star}/M_{\odot}=10^{10}$ – 10^{11} galaxies, including Borthakur et al. (2013), Werk et al. (2013), Bordoloi et al. (2014), and Lehner et al. (2020) alongside our COS-Holes detections. Each observation is colored by its corresponding SMBH mass, whether that be their dynamically measured BH mass or estimated using Equation (2). The dark-gray line is a linear regression fit for the combined COS-Holes+Literature sample and is characterized by Equation (3) with the shaded-gray region representing a 95% confidence interval. We find there is a wide scatter in the COS-Holes+Literature radial profiles as impact parameter increases. From this relation alone, we see very little observational evidence that feedback from an SMBH heavily impacts the ionization state of its CGM.

4.2. COS-Holes and Archival Data

To examine if a relationship dependent on BH mass is observable in the radial profile, we show $\log_{10}N_{\rm C~IV}$ versus impact parameter for COS-Holes and the 12 additional literature observations (Section 3) in Figure 4. Similar to Figure 3 the COS-Holes observations are represented by the circles and the literature observations are depicted as stars; all the observations are colored by their SMBH masses. $\log_{10}N_{\rm C~IV}$ weakly declines with the impact parameter within 150 kpc, a trend that has been discussed in a number of previous works (e.g., Bordoloi et al. 2014). Although there is significant scatter (>1 dex) in the

combined samples, we find that the average C IV column density of the literature sample detections (average $\log_{10}N_{\rm C~IV,Lit}=13.98\pm0.08~{\rm cm}^{-2}$) is comparable to the average C IV column density of the COS-Holes sample (average $\log_{10}N_{\rm C~IV,COS-Holes}=13.94\pm0.09~{\rm cm}^{-2}$). We find a 52% covering fraction for galaxies in the combined sample with C IV absorption above $\log_{10}N_{\rm C~IV}=13.5~{\rm cm}^{-2}$.

To characterize the radial profile for the combined samples and get a quantifiable constraint on the observed scatter mentioned above, we fit the relation between impact parameter and column density with a linear model (the dark-gray line, where the shaded-gray region represents the 95% confidence

intervals). The mean column density at some R_{proj} is:

$$\log_{10} N_{\text{C IV}}/\text{cm}^{-2} = \alpha R_{\text{proj}}/\text{kpc} + \beta.$$
 (3)

From examining the distribution of column density measurements in narrow $R_{\rm proj}$ ranges in Figure 4, it is clear that there is column density scatter beyond what can be explained by the observational uncertainties. We model this additional scatter about the \log_{10} mean column density trend as a Gaussian distribution with mean zero and standard deviation σ . The prior probability distributions over these parameters are:

$$\alpha \sim \text{Normal}(0, 1^2)$$
 (4)

$$\beta \sim \text{Uniform}(10, 16)$$
 (5)

$$\sigma \sim \text{Gamma}(2, 4),$$
 (6)

where the gamma distribution parameters are the shape and rate, respectively. The priors over α and β are broad but not infinite. The prior over σ is moderately informative: it has a mean of 1/2 and a standard deviation of $1/\sqrt{2} \approx 0.7$.

The data set includes three kinds of measurements that require different likelihood functions: detections, upper limits, and lower limits. The likelihood for a detection is assumed to be a normal distribution with known mean and standard deviation. The result of convolution with the scatter term is also a normal distribution. The likelihood for an upper limit is an improper uniform distribution between negative infinity and the upper-limit value. The convolution with the scatter term is the cumulative distribution function of a normal distribution with the mean column density trend and standard deviation σ . The likelihood and convolution with the scatter term for lower limits are similar to those of upper limits, but done in the opposite direction.

We implement this model using the NumPyro²² probabilistic programming library, which relies on JAX²³, and ArviZ.²⁴ To infer values of α , β , and σ , we run Markov Chain Monte Carlo using the No-U-Turn Sampler (NUTS) and collect samples from the posterior probability distribution. The best-fit coefficients with 95% confidence intervals are $\alpha = -0.0057$ (-0.016, 0.0042) and $\beta = 14.08$ (13.08, 14.93), respectively. Using this linear model we place constraints on the scatter in the combined COS-Holes+Literature sample and find that the slope of this relation is consistent with zero within error bars.

4.2.1. Is sSFR Directly Linked to the C IV Content of the CGM?

To investigate the possible trend suggested in Figure 3 between column density and other galaxy properties, we present the combined COS-Holes+Literature sample in three different ways as shown in Figure 5. In the top-left panel we investigate sSFR as a function of black hole mass colored by $\Delta \log_{10}N_{\rm C\ IV}$. These $\Delta \log_{10}N_{\rm C\ IV}$ values, which marginalize the large scatter in the radial profile (Section 4.2), were calculated by subtracting the observed column densities by values estimated from the best-fit line depicted in Figure 4 (Equation (3)) and is characterized by the following equation:

$$\Delta \log_{10} N_{\text{C IV}} = \log_{10} N_{\text{C IV,obs}} - \log_{10} N_{\text{C IV,Eq3}}.$$
 (7)

We choose to color the data using these corrected column densities to normalize the observations with respect to impact parameter for the combined sample so we can focus on only four parameters: sSFR, $M_{\rm BH}$, M_{\star} , and $N_{\rm C~IV}$. A similar relation is shown in the topright panel, where we present sSFR as a function of black hole mass normalized by stellar mass colored by $\Delta \log_{10} N_{\rm C~IV}$. In both of the top panels there is a clear branching occurring at $\log_{10} M_{\rm BH} > 7.0$ ($\log_{10} (M_{\rm BH}/M_{\star}) \gtrsim -3.5$); galaxies that have a $\log_{10} {\rm sSFR}$ greater than -11.0 appear to have an excess of C IV column density, while galaxies that have a $\log_{10} {\rm sSFR}$ less than -11.0 seem to have much lower C IV column densities.

However, when we show sSFR as a function of $\Delta log_{10}N_{C\ IV}$ colored by black hole mass in the bottom panel, we see that this branching falls away to reveal a correlation between sSFR and column density. We fit a linear regression to this relation, using the same method and packages as described for Equation (3), and it is characterized by the following equation:

$$\log_{10} \text{sSFR/yr}^{-1} = \alpha \Delta \log_{10} N_{\text{C IV}} / \text{cm}^{-2} + \beta.$$
 (8)

The best-fit coefficients with 95% confidence intervals are $\alpha=1.8$ (1.1, 2.5) and $\beta=-11.30$ (-11.74, -10.88), respectively. Within this relation, we do not see any trends with respect to black hole mass, suggesting that the CGM properties are only loosely tied to black hole growth, if at all. In the CGM of our combined sample, the sSFR is more closely coupled with conditions in galactic atmospheres. Since CGM properties vary as a function of galaxy properties in various and complex ways, quantifying which of these is the primary driver of the ionization state is challenging. We present two methods of analysis in which we attempt to quantify the correlations seen within the combined sample, so we can further build our understanding of how CGM properties scale with galaxy properties.

4.2.2. Bayesian Analysis

To examine the effect of R_{proj} , sSFR, M_{\star} , and M_{BH} on the C IV column density at increasing impact parameter, we perform several multivariate linear regression analyses. Building upon the Bayesian linear regression model discussed in Section 4.2, we include the galaxy properties mentioned above. We center $\log_{10} \text{sSFR/yr}^{-1}$, $\log_{10} M_{\star}/M_{\odot}$, and $\log_{10} M_{\rm BH}/M_{\odot}$ at -11.0(typical dividing point between star-forming and quenched galaxies), 10.5 (middle of the range for the combined sample), and 7.0 (middle of the range for our combined sample and point at which branching is seen in top panels of Figure 5), respectively. This operation makes the intercept β more interpretable but has essentially no effect on the linear relation slopes. We also divide R_{proj} by 100 ($R_{\text{proj},100}$) so that all properties used in the regression would have a similar dynamic range. In addition, we acknowledge that there are some upper-limit $M_{\rm BH}$ estimations for a few of our galaxies in the combined sample; however, our multivariate linear regression treats these as detections; due to the error bars for these upper limits, this should not affect the best fit in a substantial way. The equation for our multivariate regression is described by the following:

$$\log_{10} N_{\text{C IV}}/\text{cm}^{-2} = \alpha R_{\text{proj},100}/\text{kpc} + \gamma \log_{10}(\text{sSFR} - (-11.0))/\text{yr}^{-1} + \delta \log_{10}(M_{\star} - 10.5)/M_{\odot} + \epsilon \log_{10}(M_{\text{BH}} - 7.0)/M_{\odot} + \beta.$$
 (9)

Looking at the best-fit mean coefficients and their standard deviations, given in Table 4, we can immediately rule out strong

https://github.com/pyro-ppl/numpyro

https://jax.readthedocs.io/en/latest/

²⁴ https://doi.org/10.5281/zenodo.10436212

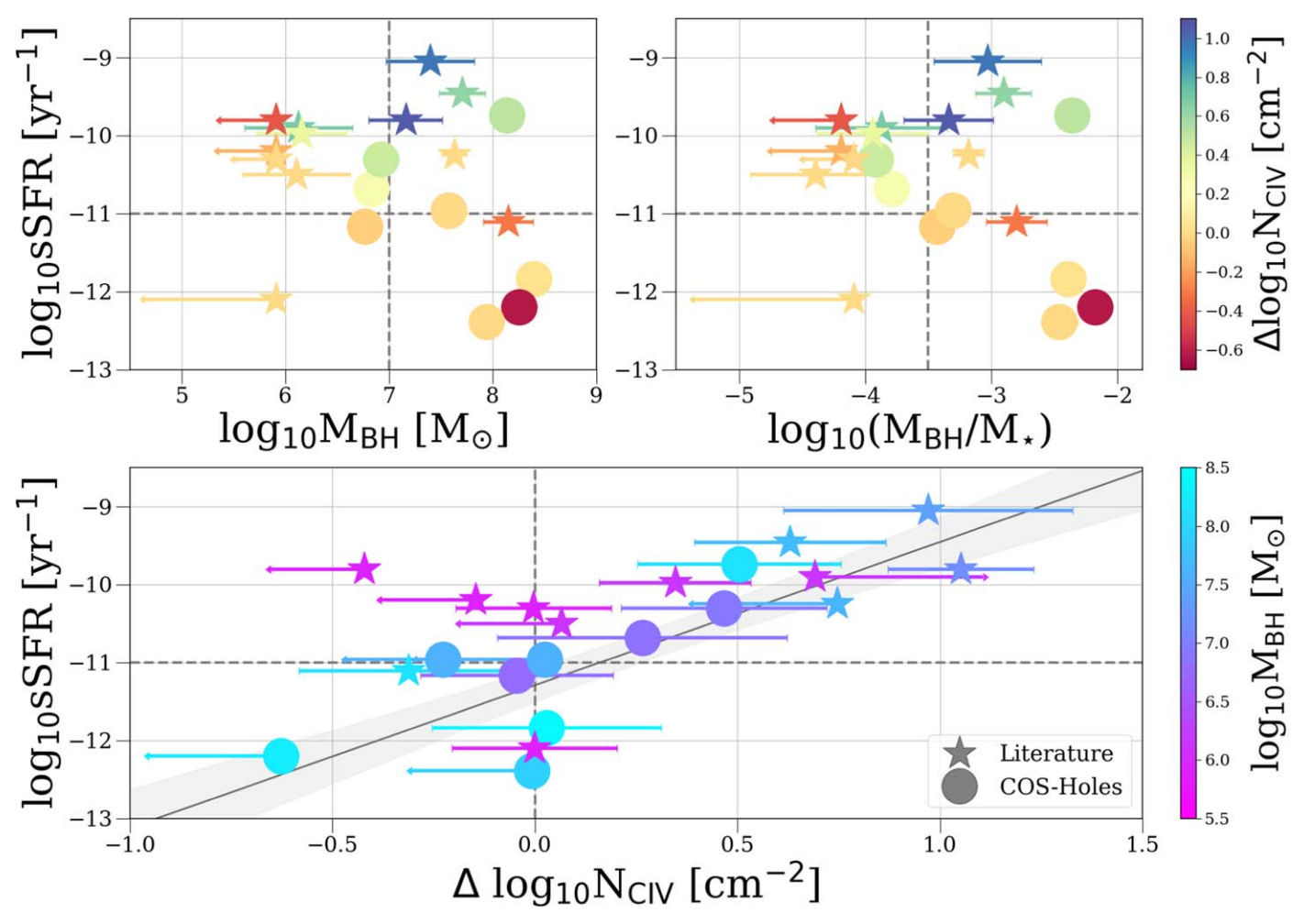


Figure 5. Investigating the role sSFR plays in driving the ionization content of the CGM across the combined sample's range of SMBH masses. Top panels: $log_{10}SFR$ as a function of $log_{10}M_{BH}$ (left panel) and $log_{10}M_{BH}$ normalized by the stellar mass (right panel) colored by $\Delta log_{10}N_{CIV}$ (C IV column density corrected for impact parameter). We present our upper-limit observations that have higher column densities than those predicted by our model (Equation (8)) as having a $\Delta log_{10}N_{CIV}$ of zero (yellow coloring). Stars with arrows pointing to the left represent upper limits on the $log_{10}M_{BH}$ estimations; for a more detailed description of how these BH masses were estimated, see Section 3. Bottom panel: $log_{10}SFR$ as a function of $\Delta log_{10}N_{CIV}$ colored by $log_{10}M_{BH}$. The dark-gray line is a linear regression, similar to the fit for Figure 4, and characterized by Equation (8) with 95% confidence intervals (the shaded-gray region). This strong correlation between sSFR and C IV suggests that sSFR is more closely tied to the ionization state of the CGM than the BH mass.

correlations with $\log_{10} M_{\star}$ and $\log_{10} M_{\rm BH}$. Both of these parameters' mean coefficients have significance less than 1σ and are unlikely to be driving the regression or impacting the ionization. The most dominant galaxy parameter, which is greater than zero with a significance of nearly 3σ , is $\log_{10} {\rm sSFR}$ and is likely the main driving component in this relation. To test this assertion, we run a similar multivariate linear regression, but only including $R_{\rm proj}$ and sSFR, where the coefficients and statistics are shown in the bottom half of Table 4, and it is characterized by the following equation:

$$\log_{10} N_{\rm C\,IV}/{\rm cm}^{-2} = \alpha R_{\rm proj,100}/{\rm kpc} + \gamma \log_{10}({\rm sSFR} - (-11.0))/{\rm yr}^{-1} + \beta.$$
 (10)

This relation is shown in Figure 6 as the gray line with its 95% confidence intervals depicted as the gray-shaded regions. The coefficients and standard deviations for the new regression remain essentially the same with $\log_{10} M_{\star}$ and $\log_{10} M_{\rm BH}$ removed, confirming that they are subdominant in setting the ionization content of the CGM of our combined sample. This is further demonstrated by the other multivariate linear

 Table 4

 Multivariate Linear Regression Coefficients

| Coeff. | Mean | σ | 95% CI |
|---|------------|----------|----------------|
| (1) | (2) | (3) | (4) |
| | Equation (| (9) | |
| α (slope) | -0.87 | 0.49 | (-1.85, 0.09) |
| γ (log ₁₀ sSFR coeff.) | 0.57 | 0.21 | (0.16, 0.98) |
| $\delta (\log_{10} M_{\star} \text{ coeff.})$ | -0.57 | 0.88 | (-3.20, 1.25) |
| $\epsilon (\log_{10}M_{\rm BH} {\rm coeff.})$ | 0.26 | 0.33 | (-0.43, 0.76) |
| β (intercept) | 14.04 | 0.44 | (13.14, 14.88) |
| | Equation (| 10) | |
| α (slope) | -0.84 | 0.45 | (-1.73, 0.05) |
| γ (log ₁₀ sSFR coeff.) | 0.49 | 0.17 | (0.17, 0.84) |
| β (intercept) | 14.13 | 0.38 | (13.37, 14.89) |

Note. Comments on columns: (1) coefficient; (2) mean coefficient value; (3) standard deviation; (4) 95% confidence intervals.

regressions included in Figure 6 where $\log_{10}N_{\rm C~IV}$ is plotted as a function of $R_{\rm proj,100}$ colored by $\log_{10}{\rm sSFR}$; each line evaluates a single fit for column density as a function of $R_{\rm proj,100}$ at

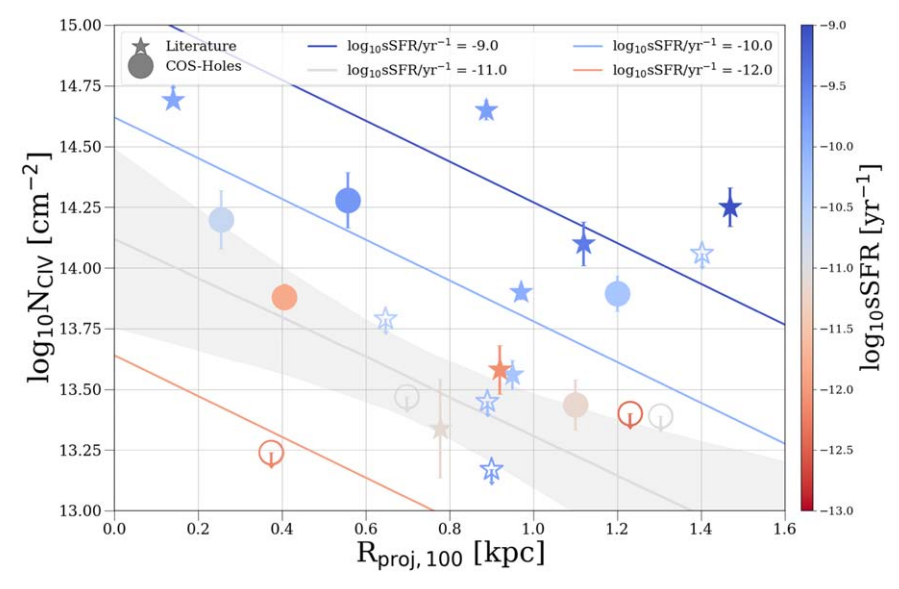


Figure 6. C IV column density as a function of $R_{\text{proj},100}$ colored by \log_{10} sSFR for the COS-Holes+Literature sample. The gray line is characterized by Equation (10) and has 95% confidence intervals depicted as the gray-shaded regions. The other solid lines represent an evaluation of a single fit for column density as a function of $R_{\text{proj},100}$ at different values of \log_{10} sSFR. The value of \log_{10} sSFR is denoted by its color and label. As \log_{10} sSFR increases from -9.0 to -12.0, the regression intercept increases and closely follows the gradient of the observations. This is further evidence showing how dominant sSFR is within the combined sample.

different values of log₁₀sSFR. As the value of sSFR increases, the regression intercept increases and changes the relation substantially, and follows the gradient of the observations, showing how dominant sSFR is within the combined sample. Based on the strong correlation seen in Figure 5, we suggest that sSFR of a galaxy is directly linked to the C IV content of the CGM.

4.2.3. Frequentist Analysis

We also investigate the relationship between $\log_{10}N_{\rm C\,IV}$, $\log_{10}M_{\rm BH}$, and $\log_{10}{\rm sSFR}$ using frequentist nonparametric tests. We first use Kendall's rank correlation test (also known as a τ test) to check for a dependence between column density and black hole mass. Specifically, we use the cenken function in the NADA R package (Lee 2020), which can handle censoring (i.e., nondetections). The test p-value for a correlation between $\log_{10}N_{\rm C\,IV}$ and $\log_{10}M_{\rm BH}$ is greater than 0.05, indicating no evidence for a dependence. The test p-value for $\log_{10}N_{\rm C\,IV}$ and $\log_{10}{\rm sSFR}$ is 0.017, which would correspond to about 2.3σ for a normal distribution: a somewhat significant correlation.

We repeat these tests on an impact-parameter-trend-corrected column density, $\Delta \log_{10} N_{\rm C~IV}$. The cenken function in NADA provides the Akritas–Theil–Sen estimator for the slope and the Turnbull estimator for the intercept of the linear relation between two variables. We use this functionality to determine the linear relation between $\log_{10} N_{\rm C~IV}$ and $R_{\rm proj}$, use that linear relation to get a predicted $\log_{10} N_{\rm C~IV}$ for each observation, and subtract that from the observed value to get $\Delta \log_{10} N_{\rm C~IV}$. We then run Kendall's rank correlation tests from the previous paragraph replacing $\log_{10} N_{\rm C~IV}$ with $\Delta \log_{10} N_{\rm C~IV}$.

For $\Delta \log_{10} N_{\rm C~IV}$ and $\log_{10} M_{\rm BH}$, we find a τ of 0.33 and a p-value of 0.85; for $\Delta \log_{10} N_{\rm C~IV}$ and $\log_{10} {\rm sSFR}$ we find a τ and p-value of 0.40 and 0.0094, respectively. The results for $N_{\rm C~IV}$ and $\Delta \log_{10} N_{\rm C~IV}$ are comparable and consistent with results from Section 4.2.2, where we see no correlation between C IV column density and black hole mass, but there is a possible correlation with sSFR. This further supports our earlier

conclusion that the SMBH does not have as significant an effect on the state of the CGM as predicted, and that sSFR, with the stronger correlation, is more directly linked with the C IV content of the CGM.

4.3. Minimum Mass of Carbon in the CGM

Following the methods used in Bordoloi et al. (2014), we estimate the carbon mass in the CGM around our sample of $\sim L^{\star}$ galaxies. Bordoloi et al. (2014) obtained their upper limit on carbon mass ($M_{\rm carbon}$) by applying a conservative ionization correction (assuming $f_{\rm C\ IV}=0.3$) to their values of C IV mass ($M_{\rm C\ IV}$); these estimates were made by assuming ionization equilibrium and including collisional- and photoionization using the CLOUDY photoionization code (Ferland et al. 1998; Chatzikos et al. 2023). The minimum carbon mass can be written as:

$$M_{\text{carbon}} \gtrsim 1.12 \times 10^6 \,\mathrm{M}_{\odot} \left(\frac{N_{\text{CIV,mean}}}{10^{14} \,\mathrm{cm}^{-2}}\right) \times \left(\frac{R_{\text{proj}}}{110 \,\mathrm{kpc}}\right)^2 \times \left(\frac{0.3}{f_{\text{CIV}}}\right) \times C_f.$$
 (11)

This calculation assumes that these galaxies conform to global stellar metallicity relations and the gas-phase mass-metallicity relation.

Inserting typical values for the COS-Holes sample, $R_{\rm proj} = 140 \, \rm kpc$, covering fraction $C_f = 44\%$, and mean column density of our detections $N_{\rm C\,IV,mean} = 10^{13.94} \, \rm cm^{-2}$, we get a minimum mass of $M_{\rm carbon}/M_{\odot} = 7.41 \times 10^5.^{25}$ This is about a factor of 2.5 lower than the $M_{\rm carbon}$ value presented in Bordoloi et al. (2014) found for both star-forming and non-star-forming dwarf galaxies using Voigt profile fitted $N_{\rm C\,IV}$ (1.9 × 10⁶ M_{\odot}). Comparing this value to the total carbon mass in the ISM of L^{\star} galaxies, we find that our minimum carbon mass is approximately a factor of 3 lower (e.g., Peeples et al. 2014).

 $[\]overline{^{25}}$ All C_f values are determined above $\log_{10}N_{\text{CIV}} = 13.5 \text{ cm}^{-2}$.

We repeated this calculation for the whole COS-Holes +Literature sample ($R_{\rm proj}=150~{\rm kpc}$, covering fraction $C_f=52\%$, and mean column density of our detections $N_{\rm C~IV,~mean}=10^{13.98}~{\rm cm}^{-2}$) and just the star-forming galaxies ($\log_{10}{\rm sSFR/yr}^{-1}\geqslant-11$) in the COS-Holes+Literature sample ($R_{\rm proj}=150~{\rm kpc}$, covering fraction $C_f=60\%$, and mean column density of our detections $N_{\rm C~IV,mean}=10^{14.17}~{\rm cm}^{-2}$) to find a minimum mass of carbon for both samples to be $1.11\times10^6~M_\odot$ and $1.98\times10^6~M_\odot$, respectively. These values are comparable to those reported in Bordoloi et al. (2014); the combined COS-Holes+Literature sample has a carbon mass 1.7 times lower than the value reported for both star-forming and non-star-forming galaxies ($1.9\times10^6~M_\odot$), while the star-forming-galaxy-only combined sample has a carbon mass only a factor of 1.3 lower ($2.6\times10^6~M_\odot$).

5. Simulation Results

In this section we compare the observational results of the combined COS-Holes+Literature sample to results from simulations. The section proceeds as follows: we describe the three simulations in Sections 5.1.1, 5.1.2, and 5.1.3 and discuss their various C IV column density predictions in Section 5.2; we compare the combined COS-Holes+Literature sample to simulated values from our three simulations in Section 5.3; and in Section 5.3.1 we mimic the COS-Holes Survey across all three simulations used in Section 5.3.

5.1. Simulation Descriptions

Here, we briefly describe the three simulations to which we will compare our results. For more details on these well-known and widely used simulations, we refer the reader to the citations referenced throughout these sections.

5.1.1. Evolution and Assembly of GaLaxies and their Environments (EAGLE)

We compare our observations to a sample of galaxies from the EAGLE main "Reference" simulation volume (Ref-L100N1504), originally published in Crain et al. (2015) and Schaye et al. (2015). This (100 comoving Mpc)³, 1504³ dark matter and smooth particle hydrodynamic (SPH) particle run uses a heavily modified version of the *N*-body code GADGET (Springel 2005). EAGLE applies the pressure-entropy SPH formulation from Hopkins (2013) and extra parameters referred to as ANARCHY (Schaye et al. 2015), and assumes cosmology from the Planck Collaboration et al. (2013; $\Omega_m = 0.307$, $\Omega_\Lambda = 0.693$, $H_0 = 67.77 \, \mathrm{km \, s^{-1} \, Mpc^{-1}}$). The initial dark matter and SPH particle masses are $9.7 \times 10^6 M_{\odot}$ and $1.8 \times 10^6 M_{\odot}$, respectively.

EAGLE implements the following subgrid physics modules: radiative cooling (Wiersma et al. 2009a), star formation (Schaye & Dalla Vecchia 2008), stellar evolution and metal enrichment (Wiersma et al. 2009b), stellar feedback (Dalla Vecchia & Schaye 2012), BH formation accretion, and feedback (Booth & Schaye 2009; Rosas-Guevara et al. 2015). In regards to the black holes, EAGLE follows BHs from seed black hole particles with mass $10^5 \, h^{-1} \, M_{\odot}$ (where h = 0.6777) placed at the center of every halo that exceeds a mass of $10^{10} \, h^{-1} M_{\odot}$. The BH particles grow via Bondi & Hoyle (1944) gas accretion as well as mergers with other BHs using the prescription derived by Booth & Schaye (2009). Stellar and BH feedback operate via thermal prescriptions that heat

surrounding gas to $10^{7.5}$ K and $10^{8.5}$ K, respectively. Further information on these processes and their calibrations is described in Crain et al. (2015).

The BH energy feedback rate is calculated by tracking the accretion rate onto BHs using the efficiency

$$\dot{E}_{\rm BH} = \frac{\epsilon_f \,\epsilon_r}{1 - \epsilon_r} \dot{M}_{\rm BH} c^2 \tag{12}$$

where $\epsilon_r = 0.1$ is the radiative efficiency of the accretion disk and $\epsilon_f = 0.15$ is the thermal feedback efficiency. The combined efficiency prefactors result in a total BH efficiency of 1.67% of the rest-mass energy accreted onto the BH. The BH feedback operates via a single-mode thermal prescription that heats surrounding gas particles to $10^{8.5}$ K. Energy is stored until a gas particle or particles can be heated to this temperature to ensure that the feedback is numerically efficient.

5.1.2. Romulus25

We also compare our observations to galaxies from the cosmological volume ROMULUS25 (R25; Tremmel et al. 2017). The ROMULUS25 $(25 \text{ Mpc})^3$ volume was run with a Λ CDM cosmology from Planck Collaboration et al. (2016) with $\Omega_0 = 0.3086$, $\Lambda = 0.6914$, h = 0.67, and $\sigma_8 = 0.77$. R25 is run using the smooth particle hydrodynamics code Charm Nbody GrAvity Solver (ChaNGa Menon et al. 2015). ChaNGa adopts the same models as GASOLINE (Wadsley et al. 2004, 2017), including the following physical prescriptions: cosmic UV background (Haardt & Madau 2012), star formation (using a Kroupa 2001 initial mass function), and blast-wave supernova feedback (Ostriker & McKee 1988; Stinson et al. 2012), which includes both supernovae (SN) Ia and SN II (Thielemann et al. 1986; Woosley & Weaver 1995). R25 has a Plummer softening length of 250 pc and a mass resolution of $3.4 \times 10^5 M_{\odot}$ and $2.1 \times 10^5 M_{\odot}$ for dark matter and gas, respectively.

R25 includes independent subgrid physics modules for the black hole formation, accretion, feedback, and dynamical friction as introduced in Tremmel et al. (2017). Unlike other simulations that use a threshold halo mass to initiate a BH seeding, BH seed particles with initial mass $10^6 M_{\odot}$ are required to form in dense, extremely low-metallicity gas to better model SMBH populations across galaxy-mass scales as described in Tremmel et al. (2017, Section 5.1). The BH accretion utilizes a modified Bondi–Hoyle prescription that considers angular momentum support from nearby gas, resulting in a different physical growth model that uses fewer free parameters. Thermal feedback energy from the BH is imparted onto the 32 nearest gas particles every time step in the form

$$E_{\rm BH} = \epsilon_r \epsilon_f \dot{M}_{\rm BH} c^2 dt, \tag{13}$$

where the radiative and feedback efficiencies are $\epsilon_r = 0.1$ and $\epsilon_f = 0.02$, resulting in a total rest-mass energy efficiency of 0.2%. The energy is released every time step dt, in contrast to the EAGLE prescription that stores energy until a surrounding gas particle can be heated to its threshold energy.

To calculate the ion column densities from the Romulus25 galaxy suite, we use the public analysis software Pynbody (Pontzen et al. 2013).²⁶ Oxygen and metal enrichment from SN and winds is traced throughout the integration of the

https://pynbody.github.io/pynbody/index.html

simulation. Then, ionization states are post-processed, assuming optically thin conditions, collisional ionization equilibrium, and a Haardt & Madau (2012) UV radiation field. Finally, we create models using the CLOUDY software package (Stinson et al. 2012; Ferland et al. 2013) for varying redshift, temperature, and density to calculate individual ion fractions for each gas particle in every simulated galaxy.

5.1.3. IllustrisTNG

The last cosmological simulation that we compare our galaxies to is the IllustrisTNG simulation, hereafter TNG. The TNG simulations were run with the moving mesh code AREPO (Springel 2010), including a magnetic hydrodynamic (MHD) solver that is seeded with the cosmologically motivated initial conditions and then follows the magnetic field self-consistently (Pakmor & Springel 2013). TNG utilizes values consistent with the Planck Collaboration et al. (2016) results ($\Omega_m = 0.3089$, $\Omega_{\Lambda} = 0.6911$, and h = 0.6774).

The $(100 \text{ Mpc})^3$ TNG simulation, also known as TNG100, is the middle of the three TNG volume series, providing a balance of volume and resolution, particularly for intermediate-mass halos. The simulation implements several subgrid processes as part of the TNG model including primordial/metal-line radiative cooling on microphysical scales, star formation based on a two-phase subgrid ISM model, evolution of stellar populations and the expected chemical enrichment/mass loss, galactic-scale outflows from energy-driven, kinetic winds from stellar feedback, and the seeding, growth, and feedback from BHs (Pillepich et al. 2018). Black hole seeds with mass $8 \times 10^5 h^{-1} M_{\odot}$ are initially seeded in halos of $5 \times 10^{10} h^{-1} M_{\odot}$.

The black hole prescriptions are introduced in Weinberger et al. (2017). Their dual-model AGN model incorporates a "thermal" mode that injects thermal energy at high Eddington accretion rates and a "kinetic" mode that injects kinetic energy at low Eddington accretion rates. The feedback efficiency for the thermal mode uses $\epsilon_r = 0.1$ and $\epsilon_f = 0.2$ from Equation (12) for a total rest-mass accretion efficiency of $\sim 2\%$, which is distributed thermally over surrounding gas cells. The kinetic mode injects kinetic "pulses" at a total efficiency that can achieve ~20% of the accreted rest-mass energy (via the physical mechanism of Blandford & Znajek 1977). Randomly oriented, jet-like pulsed feedback events apply energy directionally, imparting significant momentum stored across multiple time steps to avoid dependence on the simulation time step. This low accretion rate, kinetic mode generally dominates for late growing SMBHs above a threshold mass of $M_{\rm BH}\approx 10^{8.1}\,M_{\odot}$ (Davies et al. 2020; Terrazas et al. 2020).

5.2. Simulation Predictions

Using EAGLE, Oppenheimer et al. (2020) assert that the efficiency with which an SMBH feedback energy is coupled to the CGM is critical for understanding the process of secular galaxy formation. This can be thought about in a three-step pathway: (1) the formation of the halo, (2) the rapid growth of the BH, and (3) the lifting by AGN feedback of the baryonic halo reducing the supply of fuel for star formation. The last point is evidenced by a decrease in heavy metals in the CGM (such as C IV). These results were heavily based on the work by Davies et al. (2019), who published an inverse correlation between $M_{\rm BH}$ and $f_{\rm CGM}$ in EAGLE, suggesting a link between the BH and the removal of a significant portion of gas from the

halo, essentially reducing CGM accretion and galactic star formation. Oppenheimer et al. (2020) find that the galaxy BH mass is generally a good indicator of its past feedback history at masses above $\log_{10} M_{\rm BH}/M_{\odot} \sim 7.0$. They used high-cadence snapshot outputs from the EAGLE simulation to determine that significant AGN episodes directly lift the CGM and significantly reduce (in some cases, quench) star formation on a <100 Myr timescale. Ion tracers including C IV take longer (0.5–2.5 Gyr) to respond, but this sequence generally happens at z > 1 for L^{\star} galaxies meaning that this ion is an indicator of CGM gas content by z = 0.

TNG shows a dramatic decline in the covering factor of O VI from star-forming to quenched galaxies, as presented by Nelson et al. (2018b). Davies et al. (2020) explored both TNG and EAGLE to determine how CGM mass depends on BH mass, finding that the BH feedback energy released during the low-Eddington kinetic mode in TNG is most strongly anticorrelated with the gas content of halos in the mass range corresponding to our samples explored here. Hence, the BH mass itself is not directly deterministic for baryon lifting in TNG, but the energy released during the kinetic mode is (Davies et al. 2020; Voit et al. 2024). This manifests itself in a strong anticorrelation between BH and CGM mass, but for BH masses that are above $10^8 M_{\odot}$ where kinetic mode (and therefore baryon lifting) operates in TNG. Taking these results together, BH feedback drives the results of star-forming (lessmassive BH) galaxies having higher OVI column density compared to quiescent (more-massive BH) galaxies (Nelson et al. 2018b). Hence, the driving force depleting ionized oxygen (and mostly likely C IV as well) is the ejection of mass from the CGM due to black hole feedback.

By contrast, Sanchez et al. (2019) use R25 to examine the effects of SMBH feedback and star formation history (SFH) on the column densities of OVI in the CGM of galaxies. They determine that the host galaxy's SMBH transports metal-rich gas out of the galaxy disk where metals are formed and propagates it into the CGM. From these results they posit that galaxies with lower-mass BHs (which have experienced less accretion and therefore less feedback) are likely to have a lower-metallicity CGM and vice versa for galaxies with highermass BHs leading them to have more metal-enriched material in their host CGM. Therefore, SMBH feedback impacts the total metal mass in the CGM (but not the total gas mass) and may play a critical role in galaxy quenching (Sanchez et al. 2021). In a follow-up paper, Sanchez et al. (2024) measure the SMBH masses and CGM metal content from a sample of galaxies from R25. They find higher CGM metal fractions in galaxies with more massive black holes (compared to their host's stellar dispersion). In further contrast to EAGLE and TNG, Sanchez et al. (2024) find no correlation between $M_{\rm BH}$ and f_{CGM} , indicating that in their galaxies the SMBH's influence is more local, impacting the galaxy's disk and enriching the CGM without evacuating gas from the halo.

All of these simulations support the idea that SMBHs transport gas and metals into the CGM of the host galaxy. However, they differ on their predictions of how the mass of the SMBH regulates the amount of C IV present in the CGM. The COS-Holes Survey provides the opportunity to constrain these feedback processes by comparing EAGLE, R25, and TNG predictions. Section 5.3 compares these theoretical SMBH feedback prescriptions with our observations.

5.3. Comparison to Simulations

We begin our comparison to simulations by showing the entire observed sample (COS-Holes+Literature; $\log_{10}M_{\rm BH}=5.91-8.4~M_{\odot}$) to the three simulations. In Figure 7, we split the observations into two bins divided by $\log_{10}M_{\rm BH}=7.0$, a "low"- $M_{\rm BH}$ sample (10 observations, $\log_{10}M_{\rm BH}\leqslant7.0$) and a "high"- $M_{\rm BH}$ sample (11 observations, $\log_{10}M_{\rm BH}>7.0$). This split is strategically made to take advantage of the range of BH masses that make up the combined COS-Holes+Literature sample, but to also investigate the question, "Do galaxies with similar stellar masses but hosting differing SMBH masses show different CGM metal contents?"

We first make a broad-brush comparison between data and simulations by choosing all galaxies with stellar masses between $\log_{10} M_{\star}/M_{\odot} = 10^{10} - 10^{11}$ in the three simulations and dividing the samples into two $M_{\rm BH}$ bins in Figure 7. This means that the split black hole mass is different among the simulations as they have different $M_{\rm BH}$ distributions, as discussed in Section 5.1. In EAGLE there are 1993 central galaxies at z = 0.00 with a dividing $M_{\rm BH} = 10^{7.10} \, M_{\odot}$. In R25 there are 52 central galaxies at z = 0.05 with a dividing $M_{\rm BH} = 10^{7.6} \, M_{\odot}$. In TNG there are 3049 central galaxies at z = 0.00 with a dividing $M_{\rm BH} = 10^{8.12} \, M_{\odot}$. The distribution of black hole messes for TNG. black hole masses for TNG is narrower and more massive than the distributions for EAGLE and R25; see Section 5.3.1 for more details. For EAGLE and TNG the C IV column density radial profiles were calculated using a projection along the z axis with a total depth of 2 Mpc, while for R25 they were averaged down to R_{200c} . We choose to plot the simulations' predicted column densities versus the true projected impact parameter, R_{proj} (kpc), since it is a more direct measurement that does not rely on estimations from an indirectly observable property (like using R_{proj}/R_{200c} , which uses dark matter mass).

The radial profiles shown in the top panel of Figure 7 show that the EAGLE simulation results are in reasonable agreement with the COS-Holes+Literature absorption observations. Interestingly, there is no discernible difference in the lowand high-BH-mass samples (average $\log_{10}N_{\rm C~IV}=13.6{\rm cm}^{-2}$ for both samples). We note that Oppenheimer et al. (2020) predicted an anticorrelation between C IV and $M_{\rm BH}$, but we do not see such a correlation here. This likely is a result of the slightly larger stellar mass range probed by our COS-Holes galaxy sample compared to that of Oppenheimer et al. (2020; $10^{10-11}~M_{\odot}$ versus $10^{10.2-10.7}~M_{\odot}$). Additionally, they found a measurable difference in the reduction of C IV column densities for only the highest *quartile* of BH masses, whereas here we have divided the sample into two, leading us to have similar radial profiles for the split samples.

In the middle panel of Figure 7 where the observations are compared to $N_{\rm C\,IV}$ values from R25, we see that the mean predicted column density ($\log_{10}N_{\rm C\,IV}=12.8~{\rm cm}^{-2}$) is on average ~ 1 dex below our combined sample; thus, there is little agreement between the combined sample and those predicted by R25. We see more of a difference between the low- and high-mass-sample R25 predictions than EAGLE until $\sim 90~{\rm kpc}$ where the two samples become more indiscernible. These results are comparable to averaged radial profiles presented in Figure 14 of Sanchez et al. (2024; $\log_{10}N_{\rm C\,IV}$ versus $\log_{10}(R_{\rm proj}/R_{\rm 200c})$) at the same BH mass split but are underpredicting the C IV column density observed.

For TNG, in the last panel of Figure 7, we see the largest differentiation between the low and high samples (average

 $\log_{10}N_{\rm C\,IV}=14.0$ and $13.1\,{\rm cm}^{-2}$, respectively), which reasonably overlaps with the C IV column densities for the combined sample. Interestingly, TNG has a much larger spread for their high-mass sample than any other simulation and sample. While we do see a population of low C IV values for high $M_{\rm BH}$, there is also a population with high C IV for high $M_{\rm BH}$. A fuller investigation determining why there is such a spread in C IV for high black hole masses is beyond the scope of this paper.

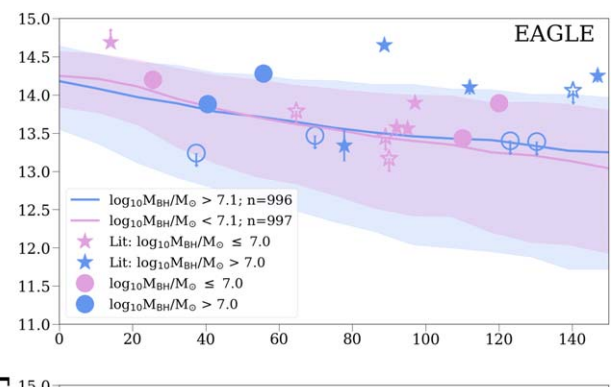
We note these general trends among each of the simulations, but we cannot directly compare them to the COS-Holes Survey without reproducing the observed survey, which we now do in Section 5.3.1.

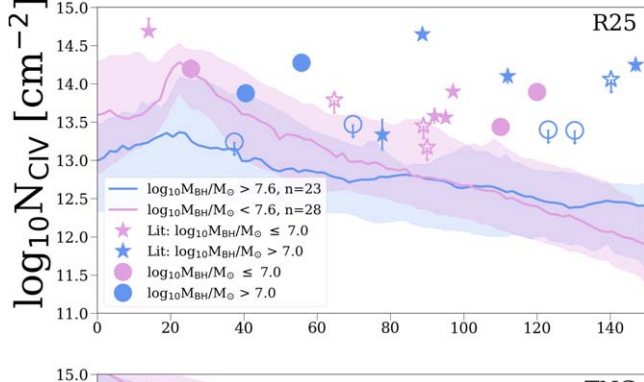
5.3.1. Mocking up the COS-Holes Survey

We create a mock-up of the COS-Holes Survey of the nine sight lines by using the SMOHALOS (Simulation Mocker Of Hubble Absorption Line Observational Surveys) used first in Oppenheimer et al. (2016) across the three simulations. In our implementation here, SMOHALOS matches the impact parameter, stellar mass, and SFR of observed galaxies using a selection of central galaxies taken from z = 0.00 simulation outputs. We also attempt to match black hole mass, but only divide the sample into two using a black hole mass split, $M_{\rm BH}$, split, that is defined differently for each simulation based on the distribution of simulated $M_{\rm BH}$ values. In SMOHALOS, the 1σ range of BH masses in EAGLE spans $10^{6.65}$ – $10^{7.94}M_{\odot}$, in R25 it spans $10^{7.27}$ – $10^{8.35}M_{\odot}$, and in TNG it spans $10^{7.94}$ – $10^{8.43}M_{\odot}$. Briefly, we choose a sight line by selecting a random pixel in a C IV column density map at an impact parameter within 5 kpc of an observed sight line around a simulated galaxy that matches the observed galaxy. We use a projection along the z axis with a total depth of 2 Mpc. SMOHALOS selects a matching simulated galaxy by taking the observed galaxy values and adding a random error assuming a Gaussian dispersion, then finding the simulated galaxy that best fits the observed galaxy's dispersed values. We assume dispersions of 0.3 dex to M_{\star} and 0.5 dex to SFR, therefore ensuring we are selecting galaxies that are similar to the COS-Holes sample but have a random scatter based on reasonable uncertainties in stellar masses and star formation rates.

We run SMOHALOS for 100 realizations, reporting the results in Table 5. We first report the median C IV column density from our observations noting the large range on the high $M_{\rm BH}$ sample due to upper limits (see Figure 3) indicating the uncertainty in which the sample has more C IV. For the simulations, we are not limited by upper limits; therefore, we present the equivalent of noiseless column densities for the median and 1σ spread in their distribution.

The first result to note is how each simulation compares with the observed data set. EAGLE has values that are consistent with both samples, R25 has values that are significantly lower than observations, and TNG agrees best with the high- $M_{\rm BH}$ sample but appears to overpredict the low- $M_{\rm BH}$ sample. In detail, TNG predicts the largest reduction in C IV with $M_{\rm BH}$, while EAGLE predicts the largest increase. This agrees with the trends in Figure 7, but we note the SMOHALOS sample as well as the split $M_{\rm BH}$ are different. By selecting matched galaxies, we are sampling a distribution that has a much smaller difference than, for example, TNG would predict for a typical galaxy in the bottom panel of that figure.





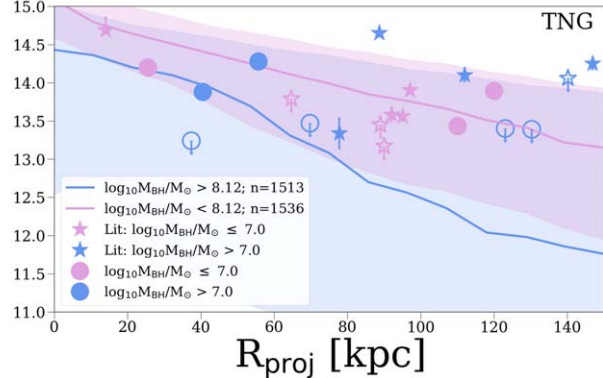


Figure 7. Column densities of the combined COS-Holes+Literature sample versus impact parameter compared to predictions from the EAGLE (top panel), R25 (middle panel) and TNG (bottom panel) simulations. Blue represents the "high"-mass black hole sample $(\log_{10}M_{\rm BH} > 7.0~M_{\odot})$ while pink refers to the "low"-mass black hole sample $(\log_{10}M_{\rm BH} \le 7.0~M_{\odot})$. The corresponding blue and pink lines are the median C IV radial profile predictions from each simulation (also split based on black hole mass), each with 16%–84% confidence spreads represented as the shaded region around each prediction. Like previous figures, unfilled markers represent an upper limit for that observation. Combined sample column densities agree reasonably with predictions from EAGLE and TNG and lie above the R25 predictions.

The second result to note is that the simulations all show 0.12 dex or less differences in their $\log_{10}N_{\rm C~IV}$ medians indicating that a COS-Holes sample is not large enough to distinguish the different behaviors across the simulations. Even if there exist different C IV absorption patterns relating to $M_{\rm BH}$, our SMOHALOS exploration finds that COS-Holes is too insensitive due to its small sample size and heterogeneous sample of galaxies.

Finally, we estimate the number of sight lines needed to distinguish between different C IV distributions as a function of BH mass by replicating the results from R25. For a set sample size, we interpolate a C IV column density from a random impact parameter (between 0 and 150 kpc) and assign it to either the low- or high-BH-mass sample to create a uniform

Table 5
SMOHALOS Simulation C IV Comparison

| Data Set | M _{BH} (split) | Low M _{BH} | High $M_{ m BH}$ |
|----------|-------------------------|----------------------------------|----------------------------------|
| 40 | (2) | $N_{\rm C\ IV}\ ({\rm cm}^{-2})$ | $N_{\rm C\ IV}\ ({\rm cm}^{-2})$ |
| (1) | (2) | (3) | (4) |
| Observed | 7.6 | 13.44-13.47 | <13.40-13.88 |
| EAGLE | 7.49 | $13.59^{+0.63}_{-1.15}$ | $13.71^{+0.53}_{-1.06}$ |
| R25 | 8.10 | $12.75^{+1.05}_{-0.77}$ | $12.78^{+0.64}_{-0.63}$ |
| TNG | 8.23 | $13.85^{+0.69}_{-1.49}$ | $13.79^{+0.78}_{-2.61}$ |

Note. Comments on columns: (1) data set, observed or simulation; (2) black hole mass used to divide sample; (3, 4) median and 1σ split for $N_{\rm C~IV}$ for low and high $M_{\rm BH}$ samples, respectively; for observations, the best estimate for median given upper limits.

sample. We fit these random replications to a linear regression model for increasing sample sizes iteratively to create a distribution. We determine that at least 60 sight lines for each high- and low-mass sample would be needed to distinguish between the samples with a 2σ confidence and over 100 sight lines in each sample to tell with a 3σ confidence.

6. Discussion

6.1. $\Delta N_{C,IV}$ Dependence on sSFR

We find a $> 2\sigma$ correlation between the impact-parametercorrected column density ($\Delta N_{\rm CIV}$) and sSFR, as shown in Figure 5. In the top panels of Figure 5, we see a distinct split in $\Delta N_{\rm CIV}$ between star-forming and non-star-forming galaxies at $\log_{10}M_{\rm BH} > 7.0$. This dividing point occurs at $\log_{10} \rm sSFR \approx$ -11.0. This is consistent with star-forming (\log_{10} sSFR >-11.0) and passive (log₁₀sSFR <-11.0) galaxies in the COS-Halos Survey (Tumlinson et al. 2011). COS-Halos found that star-forming galaxies exhibited an O VI covering fraction >80%, and higher $N_{O \text{ VI}}$ than their passive galaxy counterparts ($f_{\rm C} \approx 30\%$). Building off of these results, subsequent studies (Johnson et al. 2015; Zahedy et al. 2019; Tchernyshyov et al. 2023) have established an evident dichotomy in the amount of O VI present in star-forming and passive galaxies. Controlling for stellar/halo mass, Tchernyshyov et al. (2023) demonstrated that this dichotomy persists at high statistical significance. For the first time, we tentatively confirm with $> 2\sigma$ significance that this correlation exists in the C IV-bearing gas phase as well, even when we control for other potential variables (see Section 4 for a discussion of our multivariate analysis).

There is little C IV coverage in other surveys of L^* galaxies, and our current sample size is only 21 galaxies. The CIViL* survey (Berg et al. 2022) will fill this gap in previous COS absorption-galaxy studies by adding NUV data covering C IV for many of the L^* galaxies of COS-Halos and other surveys that also have O VI coverage. With the addition of data from this survey, we will be able to test whether C IV acts more like O VI than a tracer of the photoionized, 10^4 K gas phase. Our current sample indicates that C IV is more O VI—like than "low-ion-like," where low-ionization-state gas traced by singly and doubly ionized species shows no correlation with galaxy star-forming properties (Werk et al. 2013).

While we find a clear trend that exists between $\Delta N_{\rm C\ IV}$ and sSFR (4.2.1), we note a possible second-order connection between the sSFR and $M_{\rm BH}$ as they relate to $N_{\rm C\ IV}$ (Figure 5, top panels). As discussed above, galaxies with higher sSFRs and $M_{\rm BH}$ s show higher C IV content in the CGM, while

galaxies with similarly high black hole masses but low sSFR maintain lower C IV column densities. This split trend could indicate that the relationship between sSFR and black hole mass could result in varying $N_{\rm C\,IV}$ possibly connected to overmassive or undermassive black hole characteristics; however, other evolutionary factors such as galaxy formation time may also play a role (e.g., Sharma et al. 2020 connects overmassive black hole formation to earlier galaxy formation).

Results using EAGLE and TNG have shown that there is an inter-relationship between intrinsic galaxy halo properties and the properties of the central galaxy such as sSFR (Davies et al. 2019, 2020). In these simulations, galaxies with overmassive BHs are more likely to be quenched, and vice vera (Davies et al. 2020, Figure 2), and these quenched systems almost always have an evacuated CGM; due to the BH's influence on the CGM of the central galaxy through suppressing cooling, the total sSFR is reduced. Therefore, sSFR, BH mass (and its subsequent growth), and the CGM are highly interconnected. However, our current sample (including the additional literature values), is too small to directly test these interdependent relationships seen in simulations. Exploring whether this sSFR versus $N_{C,IV}$ trend appears in cosmological simulations could shed light on the underlying physics driving this apparent connection.

6.2. Do BHs Evacuate Their CGM?

Cosmological hydrodynamical simulation suites are now able to self-consistently recreate an array of galaxy observables (e.g., EAGLE, Schaye et al. 2015; IllustrisTNG (TNG), Pillepich et al. 2018; Romulus25, Tremmel et al. 2017), including not only the galaxy mass function but specific SMBH-related observables including the AGN luminosity function (EAGLE, Rosas-Guevara et al. 2016) and the $M_{\rm BH}$ - σ relation (IllustrisTNG, Sijacki et al. 2015; Romulus25, Tremmel et al. 2015). From these simulations, numerical and analytical calculations predict that even a small percentage of the energy from SMBH assembly, when coupled to its surrounding halo, will unbind the CGM from the dark matter halo (Davies et al. 2019; Oppenheimer et al. 2020). This evacuation of the CGM has a preventative effect such that the reduction in CGM gas density leads to long cooling times for the gas in the inner halo (Davies et al. 2020); meanwhile, this lower global gas density (not short-lived cavities or bubbles carved by AGN-mode feedback) causes galaxies to quench and stay quenched (Davies et al. 2021).

Both EAGLE (Oppenheimer et al. 2020) and TNG (Nelson et al. 2019) predict that the ionized gas in the CGM traced by C IV will be far lower density (and thus lower measured column density) in galaxies with overmassive black holes (relative to their stellar mass). By contrast, results from Sanchez et al. (2019), who used ROMULUS25 (Tremmel et al. 2017), suggest that galaxies with high-mass BHs will have higher measured column densities (higher metallicity) in their CGM due to the BH ejecting material out into the diffuse parts of the halo. The COS-Holes observations directly test these predictions to quantify the imprint of different implementations and efficiencies of BH feedback on the physical state of the CGM.

Comparing between the simulations (Figure 7), EAGLE and TNG agree better with the combined observed sample than R25. EAGLE appears to perform the best in matching the column densities of the low- $M_{\rm BH}$ sample as well as reproducing the $M_{\rm BH}$ values themselves. This may not be the case for every

ion as Nelson et al. (2018b) find TNG shows better agreement for O VI around the COS-Halos galaxies than found in EAGLE or EAGLE zoom simulations (Oppenheimer et al. 2016).

Interestingly, R25 seems to be underpredicting the observed C IV column density. The AGN feedback in R25 has been shown to be more moderate in comparison to TNG and EAGLE (Tremmel et al. 2019; Chadayammuri et al. 2021; Jung et al. 2022), possibly due to R25's lack of metal cooling. Sanchez et al. (2024) show that a result of this less powerful feedback is that the CGM of these galaxies are significantly less evacuated at these masses. However, it may be that the metalrich gas evacuated by the SMBH in these galaxies remains somewhat nearby to the galaxies, <50 kpc, as in the Milky Way mass galaxies explored by Sanchez et al. (2019), which may explain the predicted peak in $N_{\rm C~IV}$ around 30–40 kpc and the subsequent decline at high impact parameter.

Despite the combined sample reasonably aligning with EAGLE and TNG, there is no striking evidence in the COS-Holes Survey that more-massive SMBHs have lower observed column densities, which would indicate this "cleared" CGM (Oppenheimer et al. 2020) or that more-massive SMBHs have a more metal-enriched CGM due to the BH ejecting material out into the halo (Sanchez et al. 2019). However, we note that from the SMOHALOS exploration (Section 5.3.1), we do not yet have a sample large enough to determine if SMBHs are impacting the content or the ionization state of the CGM.

7. Summary and Conclusion

The COS-Holes Survey, in combination with a detailed comparison to cosmological simulations, offers the first assessment of the role of BH growth in the regulation of the baryonic content of extended gaseous halos. Broadly, our observations, when combined with data from the literature, are in reasonable agreement with simulation predictions, but do not provide definitive evidence that SMBH feedback significantly impacts the state of the CGM, either in evacuation or through metal enrichment. While our results do not rule out that a galaxy's central SMBH plays an important role in setting the state of the CGM, we find that the sSFR is more correlated with properties of the CGM. Specifically, our key results are:

- There is no identifiable relationship between the C IV content of the CGM and the mass of the assumed host galaxy's SMBH. We attribute this lack of a correlation to both the COS-Holes Survey's small sample size and the large scatter of >1 dex in C IV column density as BH mass increases.
- 2. When we augment the COS-Holes sample of eight galaxies with 12 additional galaxies from the literature for which we can estimate SMBH masses from ground-based spectroscopy and which have C IV coverage along paired QSO sight lines, we again find no significant trend between CGM C IV column densities and SMBH mass with increasing impact parameter (Figure 4).
- 3. We find that galaxy sSFR is correlated with the ionized content of the CGM as traced by C IV; this is evidenced by a large spread in sSFR for $\log_{10}M_{\rm BH} > 7.0$, where C IV strength shows clear dependence on sSFR but not $M_{\rm BH}$. Our multivariate analysis tentatively confirms, with $>2\sigma$ significance, that a correlation between sSFR and CGM C IV content exists, similar to that of CGM O VI (Tchernyshyov et al. 2023). Combined with items 1 and

2 above, our results suggest that the mass of the SMBH is a subdominant factor in the processes that contribute to the content or ionization state of the z ~ 0 CGM and that it is the galaxy sSFR that that is more tightly tied to the C IV-bearing gas phase of the CGM.

- 4. We compare C IV column densities to simulated column densities from the EAGLE, R25, and TNG simulations (Figure 7). Upon splitting the combined sample into two SMBH mass bins, we find there are only small differences in median column densities between different simulations. The combined COS-Holes+Literature sample measurements of *N*_{CIV} are in reasonable agreement with predictions from EAGLE and TNG, but are higher than predictions from R25.
- 5. We create a mock-up of the nine lines of sight from the COS-Holes Survey in all three simulations: EAGLE, R25, and TNG. We conclude that COS-Holes does not contain enough QSO-galaxy pairs to distinguish the different behaviors across all three simulations. To do so, the sample size would need to be increased from nine lines of sight to 120 lines of sight. See Section 5.3.1 and Table 5 for further details.

Since we targeted nearby, spatially extended galaxies with ancillary data (e.g., resolved Atacama Large Millimeter/ submillimeter Array and Very Large Array maps of the molecular and neutral ISM, rotation curves, stellar population ages, and metallicity gradients), our QSO spectroscopy will enable a variety of studies well beyond the scope of the goals of this paper. For example, our observed absorption-line kinematics will aid in differentiating between material recently launched from the central galaxy via feedback and gas accreting from the larger-scale environment (Bowen et al. 2016; Ho et al. 2017). Closer to the purview of the paper, this COS spectroscopy will also be crucial for differentiating between other AGN feedback prescriptions invoked in models and simulations that are in the public domain in addition to EAGLE and R25 described and used throughout this paper; these include TNG with dramatic SMBH feedback (Pillepich et al. 2018; Nelson et al. 2019) and the FIRE simulations suite (Anglés-Alcázar et al. 2017; Pandya et al. 2021). Given the significant investment in observational resources required to establish independent and well-constrained SMBH mass measurements and the rarity of UV-bright QSOs, it is unlikely that additional sight lines will become available until the next generation of extremely large telescopes and habitable worlds observatory are in active use. However, these future UV observatories will be pivotal for increasing the sample size and allowing us to test the effect of SMBH feedback on the state of the CGM.

Acknowledgments

Based on observations with the NASA/ESA Hubble Space Telescope obtained at the Space Telescope Science Institute, which is operated by the Association of Universities for Research in Astronomy, Incorporated, under NASA contract NAS5-26555. Support for Program No. HST-GO-16650 was provided through a grant from the STScI under NASA contract NAS5-26555. This research has made use of the NASA/IPAC Extragalactic Database (NED), which is operated by the Jet Propulsion Laboratory, California Institute of Technology, under contract with the National Aeronautics and Space Administration.

We thank an anonymous referee for their insightful comments that helped improve the clarity of this paper. S.L. G. recognizes the unceded traditional lands of the Duwamish and Puget Sound Salish Tribes, on which she is grateful to love and work. S.L.G. also thanks Trystyn Berg for their enlightening science discussions on this topic and their valuable input. N.N.S. acknowledges support from NSF MPS-Ascend award ID 2212959 and NASA award SMD-21-75544133. M.C.B. gratefully acknowledges support from the NSF through grant AST-2009230. KHRR acknowledges partial support from NSF grant AST-2009417. Y.F. acknowledges support by NASA award 19-ATP19-0023 and NSF award AST-2007012.

Data Availability

HST/COS spectra can be found on in MAST: doi:10.17909/njhs-4a40.

Facility: Hubble Space Telescope/Cosmic Origins Spectrograph.

Software: ArviZ (Martin et al. 2023), astropy (Astropy Collaboration et al. 2013, 2018, 2022), JAX (Bradbury et al. 2018), LIFELINES (Davidson-Pilon 2024), linetools (Prochaska et al. 2017a), matplotlib (Hunter 2007), numpy (Harris et al. 2020), NumPyro (Bingham et al. 2019; Phan et al. 2019), pandas (pandas development team 2024), pPXF (Cappellari 2023), PyIGM (Prochaska et al. 2017b), scipy (Virtanen et al. 2020), NADA (Lee 2020), veeper (Burchett 2024).

Appendix A C IV Absorption Profiles

Figure 8 presents absorption-line profiles for the COS-Holes sample. Some items of note are: (1) for NGC 4026 (QSO: SDSSJ1159) there is a prominent blend in λ 1550 that we identified corresponds to H I λ 1215 at z=0.28; due to this contamination and no features in λ 1548 we report an upper limit for the C IV column density; (2) for NGC 4258 (QSO: SDSSJ1220 and SDSSJ1222) and NGC 4564 (QSO: SDSSJ1235) we do not detect any C IV absorption and report only upper limits on C IV column density.

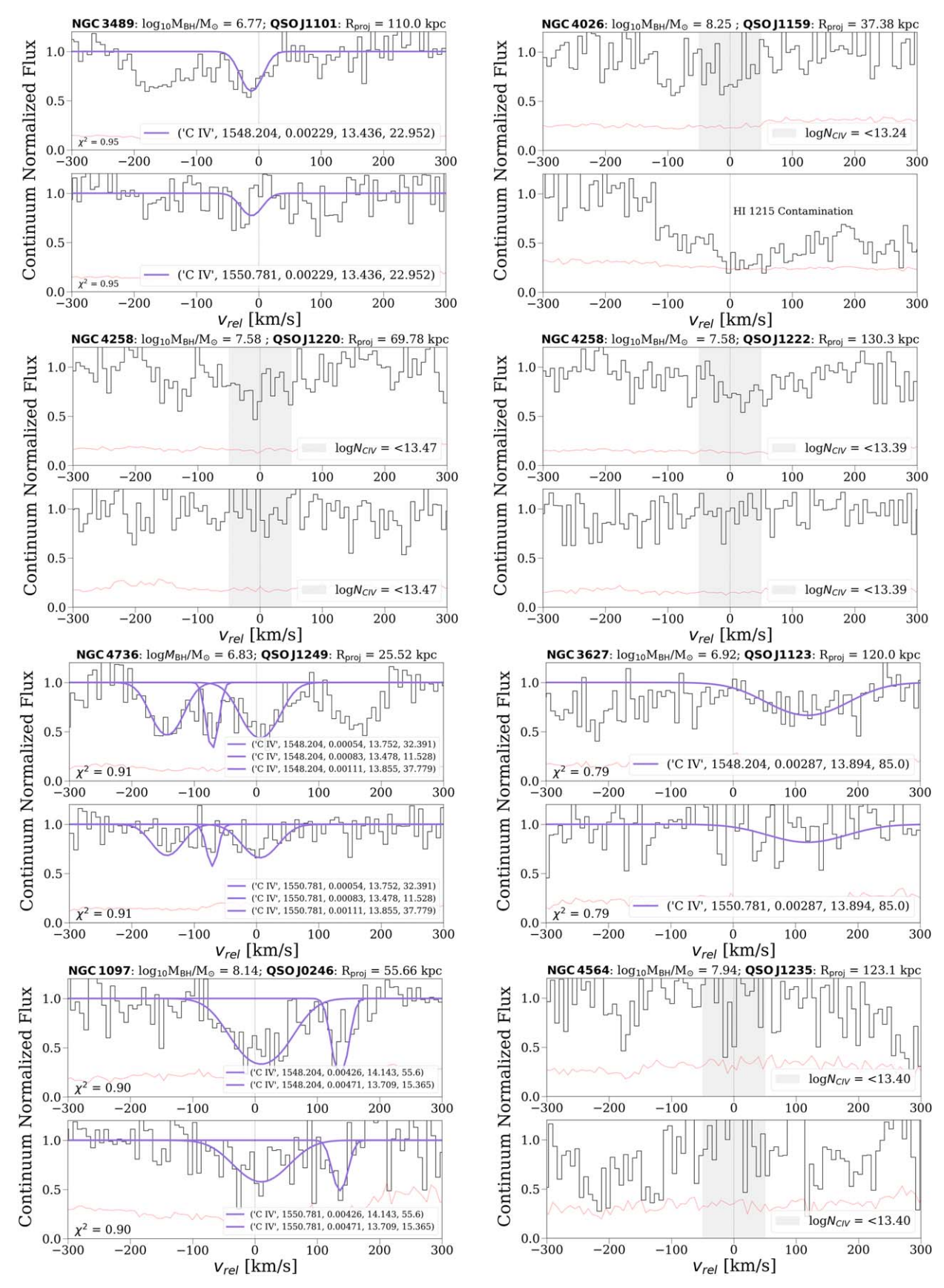


Figure 8. The remaining C IV absorption features for the COS-Holes Survey. The same conventions are used as described in Figure 2.

Appendix B Literature Sample Galaxy and QSO Tables

We increase our COS-Holes sample size by adding values from Lehner et al. (2020; Project AMIGA), Werk et al. (2013) COS-Halos), Borthakur et al. (2013; starbursts), and Bordoloi et al. (2014; COS-Dwarfs). Project AMIGA (M31; $\log_{10} M_{\star} = 9 \pm 2 \times 10^{10}$ M_{\odot} , Williams et al. $\log_{10}M_{\rm BH} = 8.15 \pm 0.24$, Davis et al. 2017; total SFR = 0.7 M_{\odot} yr⁻¹, Lewis et al. 2015) was specifically designed to span M31's projected major and minor axes and intermediate orientations; thus it provides the unique opportunity to probe one high-mass SMBH galaxy at increasing impact parameter. It is important to mention that there were data values that had possible contamination from the Magellanic Stream; however, we only plot values they denote as uncontaminated; for more a more detailed explanation of how this contamination was removed, see Lehner et al. (2020). Using this smaller sample of Project AMIGA observations, we take an average of the detections to report mean Project AMIGA column density. We use this single data point to represent the Project AMIGA observations.

We also include Borthakur et al. (2013), who found highly ionized gas traced by C IV in 80% of their starburst galaxies. They assert that it is extremely unlikely that these absorbers were photoionized from either the metagalactic background or the stellar radiation from the starburst; using CLOUDY models, they suggest that this observed C IV would arise from shock ionization and be accelerated by the ram pressure of the wind

and thus enrich the CGM. Similar high detections of C IV were seen in Bordoloi et al. (2014), where they detected the ion out to 100 kpc in their sample of sub- L^{\star} galaxies. They find that strong C IV absorption observations were detected around star-forming galaxies and they are kinematically consistent with being bound to the dark matter halos of their hosts. In conclusion, they assert that the metallic content of the CGM around their galaxy sample is best explained by the addition of strong outflows in addition to tidal debris and ram pressure stripping. Taken together, both of these archival studies support the idea that energy-driven feedback is needed to explain the presence of highly ionized ions, such as C IV, in the CGM. Thus, they are interesting samples to compare with and expand upon the COS-Holes observations.

In addition, we also include Werk et al. (2013), who presented column density measurements of the CGM from QSO-galaxy pairs (low-z, $L \approx L^*$) drawn from the COS-Halos Survey. One of their main results is finding that column densities derived for intermediate ionization state metal lines decrease with increasing impact parameter; they interpret this trend to mean there is a decline in the metal surface density profile of the CGM within its inner 160 kpc. They also see that the gas kinematics derived from Voigt profile fits to their observations suggest that the CGM is mostly bound to its host galaxy's dark matter halo, similar to results seen in Bordoloi et al. (2014). The collective information for Werk et al. (2013) and the rest of our additional literature sample can be seen in Tables 6 and 7, respectively.

 Table 6

 Literature Sample Galaxy Information

| Galaxy | R.A. (deg) | Decl. (deg) | Z | $sSFR$ $(log_{10}yr^{-1})$ | M_* $(\log_{10}M_{\odot})$ | $M_{ m BH} \ (\log_{10}\!M_\odot)$ | Ref |
|---------------------|---------------|----------------|----------|----------------------------|------------------------------|------------------------------------|-----|
| (1) | (2) | (3) | (4) | (5) | (6) | (7) | (8) |
| J102846.43+391842.9 | 157.194 | 39.312 | 0.1135 | -9.8 | 10.5 | 7.16 ± 0.35 | (a) |
| J132150.89+033034.1 | 200.462 | 3.509 | 0.0816 | -10.3 | 10.8 | 7.63 ± 0.12 | (a) |
| J140502.20+470525.9 | 211.259 | 47.091 | 0.1452 | -9.0 | 10.4 | 7.4 ± 0.43 | (a) |
| J154527.12+484642.2 | 236.363 | 48.778 | 0.0752 | -10.5 | 10.5 | 6.11 ± 0.52 | (a) |
| J0925+4535_227_334 | 141.379 | 45.533 | 0.014 | -10.3 | 10.0 | < 5.91 | (b) |
| J0959+0503_318_13 | 149.813 | 5.068 | 0.059 | -9.9 | 10.0 | 6.13 ± 0.52 | (b) |
| J1121+0325_73_198 | 170.362 | 3.445 | 0.023 | -10.2 | 10.1 | < 5.91 | (b) |
| J1211+3657_312_196 | 182.761 | 36.998 | 0.023 | -9.8 | 10.1 | < 5.91 | (b) |
| PG1202+281_165_95 | 181.183 | 27.878 | 0.051 | -12.1 | 10.0 | < 5.91 | (b) |
| J0910+1014_34_46 | 137.626 | 10.24 | 0.1427 | -9.5 | 10.61 | 7.71 ± 0.22 | (c) |
| J1619+3342_113_40 | 244.831 | 33.706 | 0.1414 | -9.9 | 10.1 | 6.16 ± 0.44 | (c) |
| M31 | 10.685 | 41.269 | -0.00099 | -11.1 | 10.9 | 8.15 ± 0.24 | (d) |

Note. Comments on columns: (1) galaxy name; (2–3) R.A. and decl.; (4) redshift of the galaxy; (5) specific star formation; (6) stellar mass; (7) black hole mass; (8) reference sample where (a), (b), (c), and (d) are Borthakur et al. (2013), Werk et al. (2013), Bordoloi et al. (2014), and Lehner et al. (2020), respectively.

Table 7Literature Sample QSO Information

| QSO | R.A. (deg) | Decl. (deg) | z | R _{proj} (kpc) | $R_{\rm proj}/R_{\rm 200c}$ | $\frac{\log_{10}N_{\rm C~IV}}{({\rm cm}^{-2})}$ | Ref |
|---------------------|---------------|----------------|-------|-------------------------|-----------------------------|---|-----|
| (1) | (2) | (3) | (4) | (5) | (6) | (7) | (8) |
| J102847.00+391800.4 | 157.2 | 39.3 | 0.473 | 88.7 | 0.52 | 14.65 ± 0.04 | (a) |
| J132144.97+033055.7 | 200.44 | 3.52 | 0.269 | 140.2 | 0.52 | <14.06 | (a) |
| J140505.77+470441.1 | 211.27 | 47.08 | 1.24 | 146.9 | 0.90 | 14.25 ± 0.08 | (a) |
| J154530.23+484608.9 | 236.38 | 48.77 | 0.399 | 64.7 | 0.37 | <13.79 | (a) |
| J09525+4535 | 141.478 | 45.596 | 0.329 | 95.0 | 0.76 | 13.56 ± 0.06 | (b) |
| J0959+0503 | 149.815 | 5.065 | 0.162 | 14.0 | 0.11 | >14.69 | (b) |
| PG1202+281 | 181.175 | 27.903 | 0.165 | 92.0 | 0.73 | 13.58 ± 0.10 | (b) |
| J1121+0325 | 170.309 | 3.43 | 0.152 | 89.0 | 0.68 | <13.45 | (b) |
| J1211+3657 | 182.811 | 36.961 | 0.171 | 90.0 | 0.68 | <13.17 | (b) |
| J0910+1014 | 137.624 | 10.237 | 0.462 | 112.0 | 0.58 | 14.1 ± 0.09 | (c) |
| J1619+3342 | 244.819 | 33.711 | 0.47 | 97.0 | 0.72 | 13.9 ± 0.03 | (c) |
| HS0033+4300 | 9.096 | 43.278 | 0.12 | 30.5 | 0.133 | 14.1 ± 0.05 | (d) |
| HS0058+4213 | 15.38 | 42.493 | 0.19 | 48.6 | 0.211 | 13.33 ± 0.18 | (d) |
| RX_J0043.6+3725 | 10.927 | 37.422 | 0.08 | 50.5 | 0.22 | 13.85 ± 0.03 | (d) |
| Zw535.012 | 9.087 | 45.665 | 0.048 | 59.7 | 0.26 | 12.99 ± 0.30 | (d) |
| RX_J0050.8+3536 | 12.711 | 35.612 | 0.058 | 77.1 | 0.335 | 13.45 ± 0.07 | (d) |
| IRAS_F00040+4325 | 1.652 | 43.708 | 0.163 | 93 | 0.404 | 13.23 ± 0.11 | (d) |
| MRK352 | 14.972 | 31.827 | 0.015 | 131.7 | 0.573 | 13.5 ± 0.15 | (d) |
| RX_J0043.6+3725 | 10.927 | 37.422 | 0.08 | 50.5 | 0.22 | <12.92 | (d) |
| RXS_J0118.8+3836 | 19.706 | 38.606 | 0.216 | 97.2 | 0.423 | <12.9 | (d) |
| RX_J0028.1+3103 | 7.045 | 31.063 | 0.5 | 139.1 | 0.605 | <13.11 | (d) |
| Project AMIGA Avg. | ••• | ••• | ••• | 77.79 | 0.33 | 13.34 ± 0.20 | (d) |

Note. Comments on columns: (1) QSO ID; (2–3) R.A. and decl.; (4) redshift of the galaxy; (5) impact parameter; (6) impact parameter normalized by the virial radius; (7) C IV column density; (8) reference sample where (a), (b), (c), and (d) are Borthakur et al. (2013), Bordoloi et al. (2014), Werk et al. (2013), and Lehner et al. (2020), respectively.

ORCID iDs Samantha L. Garza https://orcid.org/0000-0003-4521-2421

Jessica K. Werk https://orcid.org/0000-0002-0355-0134
Benjamin D. Oppenheimer https://orcid.org/0000-0002-3391-2116
Kirill Tchernyshyov https://orcid.org/0000-0003-0789-9939
N. Nicole Sanchez https://orcid.org/0000-0001-7589-6188
Yakov Faerman https://orcid.org/0000-0003-3520-6503
Kate H. R. Rubin https://orcid.org/0000-0001-6248-1864
Misty C. Bentz https://orcid.org/0000-0002-2816-5398
Jonathan J. Davies https://orcid.org/0000-0002-8337-3659
Joseph N. Burchett https://orcid.org/0000-0002-1979-2197
Robert A. Crain https://orcid.org/0000-0001-6258-0344

References

J. Xavier Prochaska https://orcid.org/0000-0002-7738-6875

Abdurro'uf, Accetta, K., Aerts, C., et al. 2022, ApJS, 259, 35
Anglés-Alcázar, D., Faucher-Giguère, C.-A., Quataert, E., et al. 2017, MNRAS, 472, L109
Asmus, D., Greenwell, C. L., Gandhi, P., et al. 2020, MNRAS, 494, 1784
Assef, R. J., Stern, D., Noirot, G., et al. 2018, ApJS, 234, 23
Astropy Collaboration, Price-Whelan, A. M., Lim, P. L., et al. 2022, ApJ, 935, 167
Astropy Collaboration, Price-Whelan, A. M., Sipőcz, B. M., et al. 2018, AJ,

Astrony Collaboration, Paletrilla, T. P. Tolland, F. L. et al. 2013, AS-

Astropy Collaboration, Robitaille, T. P., Tollerud, E. J., et al. 2013, A&A, 558, A33

Bahcall, J. N., & Spitzer, L. J. 1969, ApJL, 156, L63

Behroozi, P., Wechsler, R. H., Hearin, A. P., & Conroy, C. 2019, MNRAS, 488, 3143

Bell, E. F. 2003, ApJ, 586, 794

Bentz, M. C., & Katz, S. 2015, PASP, 127, 67

Bentz, M. C., Onken, C. A., Street, R., & Valluri, M. 2023, ApJ, 944, 29

Berg, T., Bordoloi, R., Ellison, S. L., Oppenheimer, B. D., & Werk, J. K. 2022, The C IV in L* galaxies (CIViL*) survey—Pinpointing the physical conditions and evolutionary stages of gaseous halos, HST Proposal. Cycle 30, ID., #17076

Berg, T. A. M., Ellison, S. L., Tumlinson, J., et al. 2018, MNRAS, 478, 3890 Bergeron, J. 1986, A&A, 155, L8

Bernardi, M. 2007, AJ, 133, 1954

Best, P. N., & Heckman, T. M. 2012, MNRAS, 421, 1569

Bingham, E., Chen, J. P., Jankowiak, M., et al. 2019, JMLR, 20, 28, http://jmlr.org/papers/v20/18-403.html

Blakeslee, J. P., Cantiello, M., Mei, S., et al. 2010, ApJ, 724, 657

Blandford, R. D., & Znajek, R. L. 1977, MNRAS, 179, 433

Blanton, M. R., & Roweis, S. 2007, AJ, 133, 734

Bondi, H., & Hoyle, F. 1944, MNRAS, 104, 273

Booth, C. M., & Schaye, J. 2009, MNRAS, 398, 53

Bordoloi, R., Lilly, S. J., Knobel, C., et al. 2011, ApJ, 743, 10

Bordoloi, R., Tumlinson, J., Werk, J. K., et al. 2014, ApJ, 796, 136 Borthakur, S., Heckman, T., Strickland, D., Wild, V., & Schiminovich, D.

2013, ApJ, 768, 18

Bowen, D. V., Chelouche, D., Jenkins, E. B., et al. 2016, ApJ, 826, 50

Bradbury, J., Frostig, R., Hawkins, P., et al. 2018, JAX: composable transformations of Python+NumPy programs, v0.3.13, GitHub, http://github.com/google/jax

Burchett, J. 2024, the Veeper, v1.0, Zenodo, doi:10.5281/zenodo.10993984 Burchett, J. N., Tripp, T. M., Bordoloi, R., et al. 2016, ApJ, 832, 124

Burchett, J. N., Tripp, T. M., Wang, Q. D., et al. 2018, MNRAS, 475, 2067 Cappellari, M. 2023, MNRAS, 526, 3273

Chadayammuri, U., Tremmel, M., Nagai, D., Babul, A., & Quinn, T. 2021, MNRAS, 504, 3922

Chatzikos, M., Bianchi, S., Camilloni, F., et al. 2023, RMxAA, 59, 327 Crain, R. A., Schaye, J., Bower, R. G., et al. 2015, MNRAS, 450, 1937

Crain, R. A., Schaye, J., Bower, R. G., et al. 2015, MNRAS, 450, Dalla Vecchia, C., & Schaye, J. 2012, MNRAS, 426, 140

Danforth, C. W., Keeney, B. A., Tilton, E. M., et al. 2016, ApJ, 817, 111
Davidson-Pilon, C. 2024, lifelines, survival analysis in Python, v0.28.0,
Zenodo, doi:10.5281/zenodo.10456828

Davies, J. J., Crain, R. A., McCarthy, I. G., et al. 2019, MNRAS, 485, 3783
 Davies, J. J., Crain, R. A., Oppenheimer, B. D., & Schaye, J. 2020, MNRAS, 491, 4462

Davies, J. J., Crain, R. A., & Pontzen, A. 2021, MNRAS, 501, 236

```
Davies, J. J., Pontzen, A., & Crain, R. A. 2022, MNRAS, 515, 1430
Davies, J. J., Pontzen, A., & Crain, R. A. 2024, MNRAS, 527, 4705
Davis, B. L., Graham, A. W., & Seigar, M. S. 2017, MNRAS, 471, 2187
Faerman, Y., Pandya, V., Somerville, R. S., & Sternberg, A. 2022, ApJ,
  928 37
Faerman, Y., Sternberg, A., & McKee, C. F. 2020, ApJ, 893, 82
Ferland, G. J., Korista, K. T., Verner, D. A., et al. 1998, PASP, 110, 761
Ferland, G. J., Porter, R. L., van Hoof, P. A. M., et al. 2013, RMxAA, 49, 137
Ferrarese, L., & Merritt, D. 2000, ApJL, 539, L9
Froning, C. S., & Green, J. C. 2009, Ap&SS, 320, 181
Gebhardt, K., Bender, R., Bower, G., et al. 2000, ApJL, 539, L13
Gnat, O., & Sternberg, A. 2007, ApJS, 168, 213
Green, J. C., Froning, C. S., Osterman, S., et al. 2012, ApJ, 744, 60
Haardt, F., & Madau, P. 2012, ApJ, 746, 125
Haehnelt, M. G., Natarajan, P., & Rees, M. J. 1998, MNRAS, 300, 817
Häring, N., & Rix, H.-W. 2004, ApJL, 604, L89
Harris, C. R., Millman, K. J., van der Walt, S. J., et al. 2020, Natur, 585, 357
Ho, L. C., Filippenko, A. V., & Sargent, W. L. W. 1997, ApJ, 487, 568
Ho, S. H., Martin, C. L., Kacprzak, G. G., & Churchill, C. W. 2017, ApJ,
   835, 267
Hopkins, P. F. 2013, MNRAS, 428, 2840
Hu, W., & Kravtsov, A. V. 2003, ApJ, 584, 702
Hunter, J. D. 2007, CSE, 9, 90
Johnson, S. D., Chen, H.-W., & Mulchaey, J. S. 2015, MNRAS, 449, 3263
Jung, S. L., Rennehan, D., Saeedzadeh, V., et al. 2022, MNRAS, 515, 22
Kacprzak, G. G., Vander Vliet, J. R., Nielsen, N. M., et al. 2019, ApJ, 870, 137
Kauffmann, G., Heckman, T. M., White, S. D. M., et al. 2003, MNRAS,
   341, 33
Kennicutt, R. C., & Evans, N. J. 2012, ARA&A, 50, 531
Khaire, V., & Srianand, R. 2019, MNRAS, 484, 4174
Kormendy, J., & Ho, L. C. 2013, ARA&A, 51, 511
Kormendy, J., & Richstone, D. 1995, ARA&A, 33, 581
Koss, M. J., Trakhtenbrot, B., Ricci, C., et al. 2022, ApJS, 261, 6
Kroupa, P. 2001, MNRAS, 322, 231
Läsker, R., Greene, J. E., Seth, A., et al. 2016, ApJ, 825, 3
Lee, L. 2020, NADA: Nondetects and Data Analysis for Environmental Data,
   v1.6-1.1, https://CRAN.R-project.org/package=NADA
Lehner, N., Berek, S. C., Howk, J. C., et al. 2020, ApJ, 900, 9
Lehner, N., & Howk, J. C. 2011, Sci, 334, 955
Lewis, A. R., Dolphin, A. E., Dalcanton, J. J., et al. 2015, ApJ, 805, 183
Magorrian, J., Tremaine, S., Richstone, D., et al. 1998, AJ, 115, 2285
Martin, O. A., Hartikainen, A., Abril-Pla, O., et al. 2023, ArviZ, v0.17.0,
   Zenodo, doi:10.5281/zenodo.10436212
Mathews, W. G., & Prochaska, J. X. 2017, ApJL, 846, L24
McConnell, N. J., & Ma, C.-P. 2013, ApJ, 764, 184
McQuinn, M., & Werk, J. K. 2018, ApJ, 852, 33
Menon, H., Wesolowski, L., Zheng, G., et al. 2015, ComAC, 2, 1
Miyoshi, M., Moran, J., Herrnstein, J., et al. 1995, Natur, 373, 127
Molina, M., Eracleous, M., Barth, A. J., et al. 2018, ApJ, 864, 90
Monroe, T. R., Prochaska, J. X., Tejos, N., et al. 2016, AJ, 152, 25
Nelson, D., Kauffmann, G., Pillepich, A., et al. 2018b, MNRAS, 477, 450
Nelson, D., Pillepich, A., Springel, V., et al. 2018a, MNRAS, 475, 624
Nelson, D., Pillepich, A., Springel, V., et al. 2019, MNRAS, 490, 3234
Oppenheimer, B. D. 2018, MNRAS, 480, 2963
Oppenheimer, B. D., Crain, R. A., Schaye, J., et al. 2016, MNRAS, 460, 2157
Oppenheimer, B. D., Davies, J. J., Crain, R. A., et al. 2020, MNRAS,
   491, 2939
Ostriker, J. P., & McKee, C. F. 1988, RvMP, 60, 1
Pakmor, R., & Springel, V. 2013, MNRAS, 432, 176
pandas development team 2024, pandas-dev/pandas: Pandas, v2.2.1, Zenodo,
   doi:10.5281/zenodo.10697587
Pandya, V., Fielding, D. B., Anglés-Alcázar, D., et al. 2021, MNRAS,
   508, 2979
```

```
Pâris, I., Petitjean, P., Aubourg, É., et al. 2018, A&A, 613, A51
Peeples, M. S., Werk, J. K., Tumlinson, J., et al. 2014, ApJ, 786, 54
Phan, D., Pradhan, N., & Jankowiak, M. 2019, arXiv:1912.11554
Pillepich, A., Springel, V., Nelson, D., et al. 2018, MNRAS, 473, 4077
Piotrowska, J. M., Bluck, A. F. L., Maiolino, R., & Peng, Y. 2022, MNRAS,
  512, 1052
Planck Collaboration, Ade, P. A. R., Aghanim, N., et al. 2013, A&A, 557, A52
Planck Collaboration, Ade, P. A. R., Aghanim, N., et al. 2016, A&A, 594, A13
Pontzen, A., Roškar, R., Stinson, G. S., et al. 2013, pynbody: N-Body/
  SPH analysis for python, Astrophysics Source Code Library, ascl:1305.002
Prochaska, J. X., Tejos, N., Crighton, N., et al. 2017a, Linetools/Linetools:
  Third Minor Release, v0.3, Zenedo, doi:10.5281/zenodo.1036773
Prochaska, J. X., Tejos, N. C, et al. 2017b, Pyigm/Pyigm: Initial release for
  publications, v1.0, Zenodo, doi:10.5281/zenodo.1045479
Reines, A. E., & Volonteri, M. 2015, ApJ, 813, 82
Rieke, G. H., Alonso-Herrero, A., Weiner, B. J., et al. 2009, ApJ, 692, 556
Rosas-Guevara, Y., Bower, R. G., Schaye, J., et al. 2016, MNRAS, 462, 190
Rosas-Guevara, Y. M., Bower, R. G., Schaye, J., et al. 2015, MNRAS,
  454, 1038
Saglia, R. P., Opitsch, M., Erwin, P., et al. 2016, ApJ, 818, 47
Sanchez, N. N., Tremmel, M., Werk, J. K., et al. 2021, ApJ, 911, 116
Sanchez, N. N., Werk, J. K., Christensen, C., et al. 2024, ApJ, 967, 100
Sanchez, N. N., Werk, J. K., Tremmel, M., et al. 2019, ApJ, 882, 8
Schaye, J., Crain, R. A., Bower, R. G., et al. 2015, MNRAS, 446, 521
Schaye, J., & Dalla Vecchia, C. 2008, MNRAS, 383, 1210
Sharma, R. S., Brooks, A. M., Somerville, R. S., et al. 2020, ApJ, 897, 103
Sijacki, D., Vogelsberger, M., Genel, S., et al. 2015, MNRAS, 452, 575
Silk, J., & Rees, M. J. 1998, A&A, 331, L1
Springel, V. 2005, MNRAS, 364, 1105
Springel, V. 2010, MNRAS, 401, 791
Stinson, G. S., Brook, C., Prochaska, J. X., et al. 2012, MNRAS, 425, 1270
Tchernyshyov, K., Werk, J. K., Wilde, M. C., et al. 2022, arXiv:2211.06436
Tchernyshyov, K., Werk, J. K., Wilde, M. C., et al. 2023, ApJ, 949, 41
Terrazas, B. A., Bell, E. F., Henriques, B. M. B., et al. 2016, ApJL, 830, L12
Terrazas, B. A., Bell, E. F., Pillepich, A., et al. 2020, MNRAS, 493, 1888
Terrazas, B. A., Bell, E. F., Woo, J., & Henriques, B. M. B. 2017, ApJ,
  844, 170
Thielemann, F. K., Nomoto, K., & Yokoi, K. 1986, A&A, 158, 17
Tonry, J. L., Dressler, A., Blakeslee, J. P., et al. 2001, ApJ, 546, 681
Tremmel, M., Governato, F., Volonteri, M., & Quinn, T. R. 2015, MNRAS,
Tremmel, M., Karcher, M., Governato, F., et al. 2017, MNRAS, 470, 1121
Tremmel, M., Quinn, T. R., Ricarte, A., et al. 2019, MNRAS, 483, 3336
Tumlinson, J., Peeples, M. S., & Werk, J. K. 2017, ARA&A, 55, 389
Tumlinson, J., Thom, C., Werk, J. K., et al. 2011, Sci, 334, 948
van den Bosch, R. C. E. 2016, ApJ, 831, 134
Virtanen, P., Gommers, R., Oliphant, T. E., et al. 2020, NatMe, 17, 261
Voit, G. M., Oppenheimer, B. D., Bell, E. F., Terrazas, B., & Donahue, M.
  2024, ApJ, 960, 28
Wadsley, J. W., Keller, B. W., & Quinn, T. R. 2017, MNRAS, 471, 2357
Wadsley, J. W., Stadel, J., & Quinn, T. 2004, NewA, 9, 137
Weinberger, R., Springel, V., Hernquist, L., et al. 2017, MNRAS, 465, 3291
Werk, J. K., Prochaska, J. X., Thom, C., et al. 2012, ApJS, 198, 3
Werk, J. K., Prochaska, J. X., Thom, C., et al. 2013, ApJS, 204, 17
Werk, J. K., Prochaska, J. X., Tumlinson, J., et al. 2014, ApJ, 792, 8
Wiersma, R. P. C., Schaye, J., & Smith, B. D. 2009a, MNRAS, 393, 99
Wiersma, R. P. C., Schaye, J., Theuns, T., Dalla Vecchia, C., & Tornatore, L.
  2009b, M
              RAS. 399, 574
Williams, B. F., Dolphin, A. E., Dalcanton, J. J., et al. 2017, ApJ, 846, 145
Woosley, S. E., & Weaver, T. A. 1995, ApJS, 101, 181
Yoon, J. H., Putman, M. E., Thom, C., Chen, H.-W., & Bryan, G. L. 2012,
Zahedy, F. S., Chen, H.-W., Johnson, S. D., et al. 2019, MNRAS, 484, 2257
```